



Published in final edited form as:

Cell Stem Cell. 2020 March 05; 26(3): 391–402.e5. doi:10.1016/j.stem.2020.01.008.

Distinct Mesenchymal Cell Populations Generate the Essential Intestinal BMP Signaling Gradient

Neil McCarthy^{1,2}, Elisa Manieri^{1,2}, Elaine E. Storm³, Assieh Saadatpour^{4,5}, Adrienne M. Luoma^{6,7}, Varun N. Kapoor⁸, Shariq Madha¹, Liam T. Gaynor^{1,9}, Christian Cox⁸, Shilpa Keerthivasan⁸, Kai Wucherpennig^{3,4}, Guo-Cheng Yuan^{4,5,10}, Frederic J. de Sauvage³, Shannon J. Turley⁸, Ramesh A. Shivdasani^{1,2,10,11,*}

¹Department of Medical Oncology and Center for Functional Cancer Epigenetics, Dana-Farber Cancer Institute, Boston, MA 02215, USA

²Department of Medicine, Harvard Medical School, Boston, MA 02115, USA

³Department of Molecular Oncology, Genentech, South San Francisco, CA 94080, USA

⁴Department of Data Sciences, Dana-Farber Cancer Institute, Boston, MA 02215, USA

⁵Department of Biostatistics, Harvard T.H. Chan School of Public Health, Boston, MA 02115, USA

⁶Department of Cancer Immunology and Virology, Dana-Farber Cancer Institute, Boston, MA 02215, USA

⁷Department of Immunology, Harvard Medical School, Boston, MA 02115, USA

⁸Department of Cancer Immunology, Genentech, South San Francisco, CA 94080, USA

⁹Graduate Program in Biological and Biomedical Sciences, Harvard Medical School, Boston, MA 02115, USA

¹⁰Harvard Stem Cell Institute, Cambridge, MA 02139, USA

¹¹Lead Contact

SUMMARY

*Correspondence: ramesh_shivdasani@dfci.harvard.edu.

AUTHOR CONTRIBUTIONS

N.M. and R.A.S. conceived and designed the studies. N.M. performed most experiments, with help from E.M. in crypt co-cultures and from A.M.L. for scRNA-seq. A.S. analyzed scRNA-seq data. V.N.K. and S.J.T. generated *Grem1^{Dtr}* mice. V.N.K., C.C., S.K., and E.E.S. analyzed *Grem1^{Dtr}* mice. S.M. and L.G. performed computational analyses. S.J.T. and F.J.dS. supervised *Grem1^{Dtr}* mouse studies. G.-C.Y. and K.W. supervised scRNA analyses. R.A.S. oversaw the study. N.M. and R.A.S. drafted the manuscript with input from all authors.

DATA AND CODE AVAILABILITY

Data generated in this study are deposited in GEO, with the accession number GEO:GSE130681 <https://www.ncbi.nlm.nih.gov/geo/query/acc.cgi?acc=GSE130681>. No new software code was developed for this study.

DECLARATION OF INTERESTS

E.E.S., V.N.K., C.C., S.K., F.J.d.S., and S.J.T. are employees of Genentech and own shares in Roche. The other authors declare no competing interests.

SUPPLEMENTAL INFORMATION

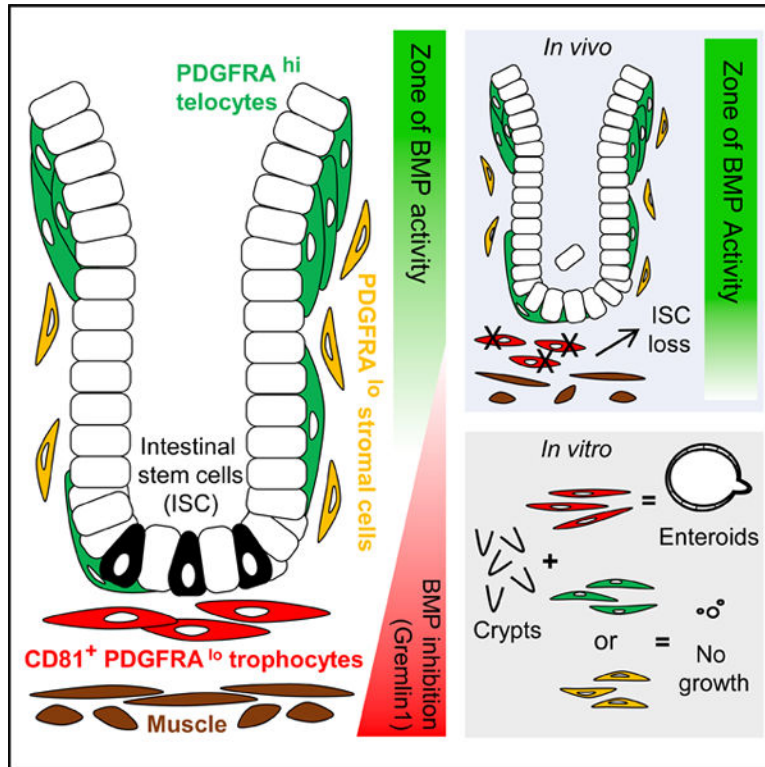
Supplemental Information can be found online at <https://doi.org/10.1016/j.stem.2020.01.008>.

Intestinal stem cells (ISCs) are confined to crypt bottoms and their progeny differentiate near crypt-villus junctions. Wnt and bone morphogenic protein (BMP) gradients drive this polarity, and colorectal cancer fundamentally reflects disruption of this homeostatic signaling. However, sub-epithelial sources of crucial agonists and antagonists that organize this BMP gradient remain obscure. Here, we couple whole-mount high-resolution microscopy with ensemble and single-cell RNA sequencing (RNA-seq) to identify three distinct PDGFRA⁺ mesenchymal cell types. PDGFRA^{hi} telocytes are especially abundant at the villus base and provide a BMP reservoir, and we identified a CD81⁺ PDGFRA^{lo} population present just below crypts that secretes the BMP antagonist Gremlin1. These cells, referred to as trophocytes, are sufficient to expand ISCs *in vitro* without additional trophic support and contribute to ISC maintenance *in vivo*. This study reveals intestinal mesenchymal structure at fine anatomic, molecular, and functional detail and the cellular basis for a signaling gradient necessary for tissue self-renewal.

In Brief

Sub-epithelial mesenchyme generates signal gradients that sustain intestinal stem cells (ISCs). McCarthy and colleagues show that anatomically and functionally distinct cells produce the BMP gradient: telocytes predominate at the crypt-villus junction and express abundant BMPs, whereas trophocytes lie near ISCs at the crypt base and express the BMP inhibitor Grem1.

Graphical abstract



INTRODUCTION

Self-renewing tissues maintain a precise balance between stem and progenitor proliferation on the one hand and terminal differentiation on the other. Much attention now centers on tissue microenvironments that underlie this balance. The small intestine lends itself well to study niche structure and function, because *Lgr5*⁺ intestinal stem cells (ISCs) and transit-amplifying progenitors reside and replicate exclusively within crypts of Lieberkühn, while their post-mitotic progeny lie along contiguous villus structures (Clevers, 2013; Potten, 1998). At the crypt-villus junction, the transition between replicating and differentiated cells is abrupt, likely reflecting local signaling centers.

ISC function and crypt cell proliferation depends on canonical Wnt ligands and their Rspodin (RSPO) co-factors (Kim et al., 2005; Kuhnert et al., 2004; Pinto et al., 2003), whereas villus cell differentiation requires bone morphogenetic protein (BMP) signaling (Chen et al., 2019; He et al., 2004; Kosinski et al., 2007). Forced BMP inhibitor (BMPi) expression in mouse intestines induces ectopic ISCs and crypts along villi (Batts et al., 2006; Davis et al., 2015; Haramis et al., 2004), indicating that BMPi specifically promote ISC activity Qi et al., 2017. Furthermore, mutations that activate Wnt signaling are obligate events in colorectal cancer (CRC) and inactivating *SMAD4* and *SMAD2* mutations, which override BMP differentiation activity, are also common somatic defects (Fearon and Vogelstein, 1990; Cancer Genome Atlas Network, 2012). Mutations that increase expression of the BMPi gene *GREM1* underlie a familial polyposis syndrome with elevated CRC risk (Davis et al., 2015; Jaeger et al., 2012). Thus, early intestinal tumorigenesis reflects liberation from physiologic constraints on Wnt and BMP signaling. In line with these physiologic signals, expansion of crypt epithelium or isolated ISCs into intestinal organoids requires recombinant (r) factors that activate Wnt and inhibit BMP signaling (Sato et al., 2009). Thus, homeostatic Wnt and BMP signals are accurately mirrored in intestinal tumors and organoid cultures.

Cells at the crypt-villus junction must therefore encounter signals that inhibit mitosis and trigger terminal differentiation. Sub-epithelial mesenchyme is a principal source of deterministic signals (Farin et al., 2012; Haramis et al., 2004; Kabiri et al., 2014), with the peri-cryptal stroma believed to create a Wnt/RSPO-enriched and BMP-poor milieu, while the villus lamina propria produces the reverse. The microenvironment is therefore classically depicted in terms of opposing gradients (Clevers, 2013; Roulis and Flavell, 2016; Sailaja et al., 2016), whose cellular basis remains obscure. Myofibroblasts (MFs) are commonly regarded as a source of trophic factors (Powell et al., 2011; Roulis and Flavell, 2016) but experimental evidence for this function is scant and, without other input, MFs may lack the heterogeneity to create sharp gradients. Recent studies implicate various mesenchymal cells as potential sources, including populations that express CD34, *FoxJ1*, PDGFRA, or *Gli1* (Aoki et al., 2016; Degirmenci et al., 2018; Greicius et al., 2018; Shoshkes-Carmel et al., 2018; Stzpourginski et al., 2015). However, the overlap and heterogeneity among these cells and functions, their roles in generating physiologic gradients, and the cellular basis of crucial BMP signal polarity remain unknown.

Using confocal microscopy of whole-mount intestinal tissue from wild-type and *Pdgfra*^{H2BeGFP} transgenic mice (Hamilton et al., 2003; Kurahashi et al., 2013), we examined the mesenchyme at high resolution. Coupled with ensemble and single-cell (sc) RNA sequencing (RNA-seq) of defined cell populations and unfractionated mesenchyme, this investigation identified likely sources of the physiologic BMP gradient: PDGFRA^{hi} telocytes embedded in the basement membrane provide a reservoir of BMP ligands at the villus base, while a distinct pool of PDGFRA^{lo} mesenchymal cells found exclusively beneath crypts expresses the surface protein CD81 and high RNA levels of the BMP inhibitor (BMPi) *Grem1*. Because the latter cells help sustain ISC *in vivo* and alone support ISC expansion into enteroid structures *in vitro*, in the absence of exogenous trophic Wnt/RSPO and BMPi factors, we call them trophocytes. Our findings thus reveal the functional architecture of an epithelial stem-cell niche, with two distinct and spatially polarized cell populations providing BMP ligands and antagonists at villus and crypt bases, respectively.

RESULTS

Stereotypic Organization of Small Intestine Mesenchyme

Mesenchymal signals responsible for intestinal epithelial self-renewal were once thought to originate largely in smooth muscle actin (SMA or ACTA2)-expressing MFs (Powell et al., 2011; Roulis and Flavell, 2016). Recent studies, however, implicate CD34⁺ (Stzepourginski et al., 2017), PDGFRA⁺ (Greicius et al., 2018), *FoxI1*⁺ (Aoki et al., 2016; Shoshkes-Carmel et al., 2018), and *Gli1*⁺ (Degirmenci et al., 2018) stromal cells as alternative sources of Wnt, RSPO, and BMP factors. We used whole-mount confocal microscopy (Bernier-Latmani et al., 2015) to resolve cell populations in the mouse small intestine. CD31⁺ capillaries abutting the basement membrane provided landmarks in each villus lamina propria, feeding into large blood vessels in the muscularis (Figure S1A). Every capillary plexus had adjacent TUJ1⁺ neuronal processes and enveloped classical SMA⁺ MFs and LYVE1⁺ lacteal vessels (Figures S1A–S1D). *Pdgfra*^{H2BeGFP} knockin mice (Hamilton et al., 2003; Kurahashi et al., 2013) revealed sub-epithelial cells in which GFP⁺ nuclei serve as a proxy for PDGFRA expression (Figure S1E). All nuclei between the capillary plexus and intestinal epithelium gave high GFP signals and were embedded in the basal lamina (Figures S1F and S1G). These cells were distinct from GFP^{hi} Purkinje-like neural cells in the muscularis (Kurahashi et al., 2012) and their PDGFRA⁺ cell membranes enveloped the mucosa from the crypt base to villus tips (Figures 1A, 1B, S1H, and S1I), indicating that sub-mucosal GFP^{hi} cells correspond to *FoxI1*⁺ telocytes (Aoki et al., 2016; Shoshkes-Carmel et al., 2018). Notably, telocyte distribution along the crypt-villus long axis is non-uniform. We did not detect enrichment in crypts, but found substantially higher cell density at the villus base and a second, lesser concentration at villus tips (Figures 1A, 1B, and S1J; Videos S1 and S2). This axial asymmetry was evident throughout the small intestine, implying that along the crypt-villus axis, secreted telocyte products concentrate at these levels.

Pdgfra^{H2BeGFP} mice revealed a second population of cells with lower GFP signals. GFP^{lo} cells in the lamina propria lie deep to the vascular plexus (Figure 1C–D), distinct from GFP^{hi} telocytes. Even around crypts, GFP^{lo} cells lie farther from the epithelium than telocytes (Figure 1E) and are plentiful between crypt bases and external muscle layers (Figure 1F). By

immunostaining and flow cytometry, GFP^{lo} cells express less PDGFRA than telocytes, outnumber the latter cells several-fold, and have an expansive cytoplasm (Figures 1E and 1G). GFP^{lo} nuclei were not associated with SMA⁺ cytoplasm or peri-endothelial NG2⁺ cells (Figures S1K–S1O), indicating that PDGFRA^{lo} cells are not MFs or pericytes. Together, these findings reveal stereotypical organization of intestinal mesenchyme, with telocytes, blood endothelium, pericytes, MFs, and lymphatic channels present at increasing distance from the mucosa. Judging by both microscopy and flow cytometry, distinctive PDGFRA^{lo} cells represent approximately a quarter of the stroma and intersperse among MFs from villus tips into the deep sub-mucosa.

Distinctive Global and Signaling Profiles of Telocytes and PDGFRA^{lo} Sub-epithelial Cells

Previous studies refer to PDGFRA⁺ sub-mucosal cells collectively as “myofibroblasts” and implicate telocytes and unfractionated PDGFRA⁺ cells as Wnt and RSPO sources, respectively (Aoki et al., 2016; Greicius et al., 2018; Shoshkes-Carmel et al., 2018). To resolve cellular identities and function, first we stripped away the external muscle to eliminate GFP^{hi} Purkinje-like cells (Figure S2A). Flow cytometry with PDGFRA antibody (Ab) detected a fraction of PDGFRA⁺ cells, especially PDGFRA^{hi} (GFP^{hi}) but discriminated the two populations less well than GFP (Figures 1G and S2B), which we used instead to purify these populations. Because endothelium supports other tissues (Ding et al., 2012; Shen et al., 2004; Yoshida et al., 2007), we also used CD31 and LYVE1 Ab to isolate blood and lymphatic endothelial cells (Figure S2C). The four transcriptomes were distinct from one another and from those of Lgr5⁺ ISC or other epithelial cells (Figures S2D and S2E). Known marker genes indicated cell purity, confirmed telocytes as unique *Pdgfra*^{hi} *Foxl1*⁺ cells, and indicated that markers recently used to isolate mesenchymal populations (Degirmenci et al., 2018; Greicius et al., 2018; Shoshkes-Carmel et al., 2018; Stzepourginski et al., 2017) are not restricted to single cell types (Figure 2A). Specifically, *Cd34* and *Pdpr* (*Glp38*) levels are highest in PDGFRA^{lo} cells and telocytes, respectively, while *Gli1* is expressed equally in these populations. Notably, PDGFRA^{lo} cells and telocytes differ in expression of >2,400 genes (Figure 2B, $q < 0.05$, log₂ fold-difference >1.5), verifying that they are distinct from one another.

Although some PDGFRA[−] cells express *Rspo3*, *Wnt2*, and *Wnt3*, as other groups have noted (Gregorieff et al., 2005; Ogasawara et al., 2018), RNAs encoding Wnt- and BMP-pathway factors are especially enriched in telocytes and PDGFRA^{lo} cells (selected transcripts shown in Figure 2C, full list in Table S1). In particular, PDGFRA^{lo} cells express the canonical ligand *Wnt2b* and three Wnt-potentiating *Rspo* factors, while telocytes mainly express non-canonical *Wnt4*, *Wnt5a*, and *Wnt5b* ligands and less *Rspo* mRNA than PDGFRA^{lo} cells; both cell types express Wnt inhibitors. Intestinal Wnt gradients are therefore not readily attributed to any cell type. In contrast, transcripts for BMP signaling were polarized, with multiple agonists present largely in telocytes. In other tissues, BMP2/7 and BMP4/7 heterodimers signal more potently than BMP2 or BMP4 homodimers (Aono et al., 1995; Kaito et al., 2018; Kim et al., 2019), and *Bmp7* transcripts are confined to telocytes. Among BMPi, *Grem1* is restricted to PDGFRA^{lo} stromal cells, while *Chrd* is expressed higher in telocytes (Figures 2C and 2D; Table S1).

Because both PDGFRA⁺ cell types express positive and negative regulators of crypt epithelium, we examined their niche functions in co-cultures with isolated crypt epithelium. In Matrigel supplemented with RSPO1 and NOGGIN, isolated crypt epithelium robustly generates organoid structures (Sato et al., 2009), and in lieu of these factors, we added 4×10^4 cells of each PDGFRA⁺ type, purified by GFP flow cytometry. Although GFP⁺ telocytes persisted in co-culture for many days, crypt epithelium routinely died within 48 h; in contrast, PDGFRA^{lo} cells robustly induced large spheroid epithelial structures (Figure 2E). Thus, GFP^{lo} cells substitute effectively for RSPO and BMPi to generate enteroid structures *in vitro*. However, the structures propagated inefficiently in serial passage (Figure S2F); we return to this point below.

Pdgfra Marks Three Distinct Mesenchymal Cell Populations

Because both PDGFRA^{lo} cells and telocytes appear throughout the crypt-villus axis, we applied single-cell (sc) RNA-seq to identify molecularly defined subpopulations. Among 2,595 PDGFRA⁺ cells, each providing information on at least 2,000 transcripts, graph-based clustering (STAR Methods) revealed 3 distinct cell types (Figure 3A). Known molecular markers identified these as *Cd34⁻ Pdgfra^{hi} Foxl1⁺* telocytes and two *Cd34⁺ Pdgfra^{lo} Foxl1⁻* subpopulations, Lo-1 and Lo-2 (Figures 3A and S3A). Further characterization revealed each population to be homogeneous and different from the others (Figure 3B). Among genes that discriminate between the three PDGFRA⁺ cell types, *Bmp5*, *Bmp7*, and *Bmp3* ranked just below *Pdgfra*; *Grem1* was the 3rd best marker of Lo-1 cells; and *Sfrp1*, a Wnt antagonist, best distinguished PDGFRA^{lo} cells from telocytes (Figures 3C and 3D; Table S2). Single-cell RNA (scRNA) analysis also revealed stark differential expression of various BMP and Wnt agonists, co-factors, and inhibitors (Figure S3B). These data thus identify two PDGFRA^{lo} populations with distinctive signaling potential. Of note, PDGFRA^{lo} cells support isolated crypt epithelium *in vitro* (Figure 2E) despite high levels of Wnt antagonist mRNAs (Figure S3B), implying again that loco-regional Wnt control has a likely complex basis.

Above, we compared PDGFRA⁺ cell transcriptomes with those of endothelial and epithelial cells (Figure 2). To study their broader relationship to the tissue, we profiled transcripts in external muscle-depleted whole small intestine mesenchyme by scRNA-seq. As expected, a large fraction of the tissue consisted of *Cd45⁺ (Ptprc⁺)* leukocytes, which we do not consider further, except for a small *Ptprc⁺* immune cluster that co-expresses *Pdgfra* and *Cd52* (Figure S4A). The remaining 3,763 cells included glial (*Gfap⁺ S110b⁺*), pericyte (*Rgs5⁺ Pdgfrb⁺*), lymphatic (*Lyve1⁺*) and blood (*Pecam1⁺*) endothelial, and *Ptprc⁺ Cd52⁺* immune cells (Figures 4A and S4B). *Pdgfra⁺* cells clustered distinctly and outnumbered all other populations, followed by MFs (*Acta2^{hi} Myh11^{hi}*). Consistent with *Pdgfra^{H2BeGFP}* histology and flow cytometry (Figure 1), *Pdgfra^{lo}* cells were in the majority (Figure 4A-B). The global analysis confirmed that *Gli1*, *Pdprn*, and other markers previously used to investigate the intestinal mesenchyme are expressed broadly (Figure 4B), and *Pdgfra^{lo}* cells form two abundant *Cd34⁺* sub-clusters, with uniformly high *Grem1* in one (Figure 4C). Of note, *Foxl1* was not confined to telocytes, but also expressed in MFs (Figure 4C); conversely, *Acta2* was not restricted to MFs, but also present in pericytes and telocytes. *Bmp7*, which is necessary in other tissues to generate active BMP heterodimers (Aono et al., 1995; Kaito et al., 2018;

Kim et al., 2019), was absent from cells other than telocytes (Figure 4C). Few cell types showed high levels of Wnt signaling factors, beyond those we identified from bulk RNA data (Figure 2) and additional Wnt inhibitors in MF, immune, and glial cells (Figure 4D). Only three canonical ligands were appreciable: *Wnt2* in lacteal endothelium, low-level *Wnt2b* in *Pdgfra*^{lo} cells and MFs, and *Wnt6* in glial cells.

To resolve the anatomic distribution of *Pdgfra*⁺ cells, we used RNA *in situ* hybridization. *Grem1*, a distinctive Lo-1 marker, was previously shown to be restricted to the deep intestinal sub-mucosa (Davis et al., 2015; Worthley et al., 2015). We found that its expression domain encompasses external smooth muscle and cells that are prominently and uniformly arrayed just below intestinal crypts (Figure 5A). In *Pdgfra*^{H2BeGFP} intestines, *Grem1* was confined to PDGFRA^{lo} cells in this location and, in agreement with absence of *Grem1* mRNA in telocytes and low expression in Lo-2 cells (Figures 3D and 4C), neither basement membrane-embedded telocytes nor PDGFRA^{lo} cells situated above and around crypts gave signals (Figure 5A). Cells lying between *Grem1*⁺ PDGFRA^{lo} cells (Lo-1) and crypt epithelium also lacked *Grem1* (Figure 5A), suggesting that any signal transmission between these compartments is likely paracrine. In contrast, *Bmp5* and *Bmp7* predominate in telocytes and concentrate at the villus base (Figure 5B), where telocytes congregate (Figure 1A). Peri-cryptal telocytes also express *Bmp* transcripts (Figure 5C), consistent with scRNA evidence for uniform *Bmp* expression in PDGFRA^{hi} cells (Figure 3D). scRNA data from whole mesenchyme confirmed that *Bmp* ligands, including *Bmp7*, predominate in telocytes (Figure 5D). These data collectively implicate telocytes as the dominant source of mesenchymal BMP signals and *Grem1*⁺ Lo-1 cells as a unique sub-cryptal population that may neutralize those signals. We propose that polarized distribution of these distinctive cells underlies the intestinal BMP gradient (Figure 5E).

Lo-1 Cells Contribute to Sustain Lgr5⁺ ISC *In Vivo* and Organoid Growth *In Vitro*

scRNA data from PDGFRA⁺ cells identified unique molecular markers. *Cd81*, which encodes a cell surface tetraspanin, best distinguished Lo-1 from other PDGFRA⁺ cells (Figure 3C; Table S2) and was useful to separate PDGFRA⁺ subpopulations, as we show below. However, *Cd81* expression in epithelial and other mesenchymal cells (Figure S4C) precludes its utility in depleting Lo-1 cells selectively. *Grem1* being more restricted (Figures 3D, 4C, 5A, and 5D), we crossed *Grem1*^{Cre-ER(T2)} mice (STAR Methods) with *Rosa26^{L-S-L}(EYFP)* reporter mice (Srinivas et al., 2001). After CRE induction, YFP was evident in SMA⁺ external muscle (cells excluded from the preceding analyses) and in SMA⁻ mesenchymal cells lying just above the muscularis (Figure S4D), in the same region as Lo-1 cells. *Pdgn* is abundant in PDGFRA⁺ cells (Figures 2A and 4B), and immunohistochemistry (IHC) and flow cytometry also localized YFP (*Grem1*) to a small PDPN⁺ fraction, as expected for Lo-1 (Figure S4E). We therefore generated *Grem1*^{Cre-ER(T2);Rosa26^{L-S-L}(DTR) mice (Buch et al., 2005), expecting tamoxifen to induce *Diphtheria* toxin (DT) receptor in *Grem1*⁺ cells. As *Grem1* is absent from the epithelium (Figures 2C and 5A), the effects of treating the mice with DT will reflect ablation of stromal cells, including Lo-1 and the external muscles, but not MFs or telocytes. Indeed, treatment of *Grem1*^{Cre-ER(T2);Rosa26^{L-S-L}(DTR) mice with DT depleted *Grem1*⁺ cells efficiently within 2 days (Figures 6A and S5A), including external muscle, but sparing PDPN⁺ cells other than}}

the *Grem1*⁺ subpopulation (Figures S5B and S5C). DT-treated mice survived 8–9 days and necropsies showed edematous intestinal dilation (Figure S5D). Histology over the preceding days showed muscle loss, leukocyte infiltration, and progressive crypt degeneration with attenuation of villus height; the ileum was affected more severely than the duodenum (Figures 6B and S5E).

ISCs, represented by the markers *Lgr5* and *Olfm4*, were substantially reduced, starting by the 2nd day after DT exposure and remaining low to absent thereafter (Figures 6C and S6A). TA cells, which normally reside above the ISC and Paneth cell zone, continued to replicate and extended into the space previously occupied by ISCs (Figure 6D). Paneth cells, which normally lie between ISCs, were also reduced, either as a direct effect of *Grem1*⁺ cell deficiency or a secondary consequence of ISC depletion, whereas goblet cells were substantially increased (Figures 6D, S5E, and S6B). Because Lo-1 cells express *Rspo* mRNAs, and PDGFRA^{lo} cells support enteroid growth without supplemental factors, we expected *Grem1*⁺ cell loss to possibly affect TA cells, but their continued replication indicates that *Grem1*⁺ cells are dispensable for Wnt-dependent TA cell proliferation. Nevertheless, the canonical Wnt target gene *Axin2* was decreased in all DT-treated *Grem1*^{Cre};*Rosa26*^{ΔDTR} mice at all times (Figure S6B). Among many possibilities, one is that *Grem1*⁺ *Rspo3*^{hi} sub-epithelial cells increase Wnt tone to the levels necessary for *Axin2* expression, while cell replication requires lesser Wnt signaling.

Our hypothesis that ISCs depend on sub-cryptal Lo1-cells for BMPi predicts increased BMP signaling in DT-treated *Grem1*^{Cre};*Rosa26*^{ΔDTR} ISC. To test this postulate, we performed *in situ* hybridization for the well-known intestinal BMP target gene *Id1* (Ogata et al., 1993; Valdimarsdottir et al., 2002). *Id1* mRNA was absent from the crypt base before DT exposure, as expected; it appeared there on day 2 in cells with ISC morphology, reflecting increased BMP signaling, and was absent thereafter, consistent with ISC attrition (Figures 6E and S6C). Together, these findings implicate some combination of sub-cryptal *Grem1*⁺ cells (i.e., Lo-1 and/or external smooth muscle) as a crucial source of BMPi *in vivo*. To interrogate the specific role of *Grem1*⁺ Lo-1 cells, we returned to enteroid co-cultures.

Lo-1 Cells (Trophocytes) Alone Sustain Organoid Growth *In Vitro*

Unfractionated PDGFRA^{lo} cells support enteroid growth (Figure 2E) and to distinguish which subpopulation carries this trophic activity, we sought to separate Lo-1 from Lo-2 cells. Among PDGFRA⁺ cells, *Cd81* is highly enriched in the Lo-1 group and flow cytometry readily separated PDGFRA^{lo} cells into CD81⁺ (Lo-1) and CD81[−] (Lo-2) fractions (Figures 7A and S4C). Isolated cells retained their molecular signatures *in vitro* (Figure S7A) and when mixed with isolated crypt epithelium, Lo-1 cells robustly expanded enteric spheroids, whereas equal numbers of Lo-2 cells allowed only a few crypts to survive but barely expand (Figure 7B). Enteroid growth was proportional to the number of CD81⁺ PDGFRA^{lo} cells (Figure S7B) and, in contrast to unfractionated PDGFRA^{lo} cells, the structures stimulated by CD81⁺ PDGFRA^{lo} cells could be passaged (Figure 7C), indicating ISC self-renewal. Because these cultures occurred in Matrigel, a matrix of unknown composition, we repeated them in collagen. Culture of crypt epithelium and CD81⁺ PDGFRA^{lo} cells in adjacent collagen droplets stimulated enteroid growth at the interface

(Figure S7C). Thus, sub-cryptal Lo-1 cells provide diffusible trophic factors sufficient to potentiate Wnt and oppose BMP signals, effectively replicating crypt conditions *in vitro*; hence we call these cells trophocytes. Unfractionated PDGFRA^{lo} cells likely failed to support long-term ISC self-renewal (Figure S2F) because factors in the dominant Lo-2 population, which lies far from the crypt bottom, limit trophocyte-induced ISC expansion.

Rspo RNA levels being more comparable in CD81⁺ and CD81⁻ PDGFRA^{lo} cells than *Grem1* RNA (Figures 4D and S3B), we asked whether a BMPi alone might explain their contrasting effects on enteroid growth. In control experiments, individual factors replicated the activities reported in the absence of other cells (Sato et al., 2009) (Figure S7D). Supplementation of CD81⁻ cell co-cultures with rNOGGIN or rGREM1 robustly stimulated enteroids, while rRSPO1 only promoted growth to the levels seen with corresponding controls (Figures 7D, 7E, and S7E). Thus, BMPi is a key niche component that distinguishes trophocytes from supra-cryptal CD81⁻ PDGFRA^{lo} cells. Supplemental rNOGGIN did not confer trophic potential on telocytes and crypts co-cultured with telocytes developed fewer spheroids with either rRSPO1 or in complete medium (Figure 7E). These findings reveal telocyte limitations in supporting spheroid growth and suggest that they may even exert suppressive effects.

DISCUSSION

Brisk self-renewal of the intestinal epithelium ensures a steady supply of short-lived enterocytes and secretory cells to digest food, secrete hormones, and resist microbial entry. The intestinal lumen is not a sterile space and microbe-induced inflammation and cell loss trigger adaptive crypt responses. Normal cell turnover and these homeostatic responses require epidermal growth factor (EGF), Wnt, BMP, and other signals secreted from the underlying stroma (Farin et al., 2012; Haramis et al., 2004; Kabiri et al., 2014), and inadequate epithelial repair is a prominent feature of inflammatory bowel disorders. Conversely, clonal ISC expansion and malignant transformation invariably reflect activating Wnt pathway mutations and are frequently associated with defects that suppress BMP signaling (Cancer Genome Atlas Network, 2012). The opposing effects of Wnt and BMP signaling on ISC and villus cells therefore predict functional gradients wherein agonists dominate near the bottom (Wnt) or top (BMP) of crypts, and inhibitory activity or absence of ligands prevails at the other end (Clevers, 2013; Roulis and Flavell, 2016; Sailaja et al., 2016; Qi et al., 2017); similar arrangements may apply to niche signals in the skin, bone marrow, and other stem cell-dependent organs. The small intestine houses unique, well-characterized tissue compartments and organoid culture allows examination of stem cell activity *in vitro*. We took advantage of both features to uncover the likely basis of the intestinal BMP gradient.

There are many possible ways to generate signaling gradients (Barkai and Shilo, 2009). For example, cells that differ only in a few specific products might secrete different factors at various points along the crypt-villus continuum. Telocytes, for example, express agonists as well as inhibitors of Wnt signaling, and investigators who recently characterized these Foxl1⁺ cells proposed such a basis for the Wnt gradient (Aoki et al., 2016; Shoshkes-Carmel et al., 2018). Alternatively, agonist and antagonist sources could be physically separate, with

diffusion of both types of molecules resulting in finely graded signaling centers. Although secreted antagonists may sharpen a signaling gradient (Barkai and Shilo, 2009), inhibitory activities are not imperative; effective gradients may form in their absence, by virtue of limited agonist diffusion (Wolpert, 1971). This study reveals simple design elements in the intestinal BMP gradient. Near crypt tops, where epithelial cells stop dividing and start to mature, the requisite BMP reservoir does not result from presence of a unique cell. Rather, ostensibly homogeneous *Pdgfra*^{hi} *Foxl1*⁺ telocytes that express BMPs and are present throughout the crypt-villus axis merely concentrate in high numbers at the villus base. To limit or preclude BMP signaling at the crypt base, the intestine seems not to rely on diffusional decay of BMPs from this source. Instead, distinctive PDGFRA^{lo} CD81⁺ trophocytes positioned beneath the ISC compartment express the BMPi *Grem1*. Counter-diffusion of telocyte-derived BMPs and trophocyte-derived GREM1 likely produces a graded signal, so that progenitor cells moving along intestinal crypts serially encounter less GREM1 and more BMPs. Notably, among all resident stromal cells, *Bmp7*, a ligand required for active BMP2/7 and BMP4/7 heterodimers in other tissues (Aono et al., 1995; Kaito et al., 2018; Kim et al., 2019), is restricted to telocytes.

CD81⁺ trophocytes represent a fraction of the PDGFRA^{lo} cell pool, expressing *Grem1* almost exclusively. mRNA data further indicate that PDGFRA^{lo} cells and telocytes are especially enriched for positive and negative regulators of various pathways, indicating that most signals pertinent to crypt-villus epithelial physiology originate in mesenchymal PDGFRA⁺ cells. We do not yet know the signaling function of abundant CD81⁻ PDGFRA^{lo} lamina propria cells or that of the telocyte-enriched compartment at villus tips; one or both populations may modulate mature cell behaviors, such as anoikis. Of note, purified telocytes express some *Rspo3*, but only non-canonical Wnt transcripts (*Wnt4*, *Wnt5a*, *Wnt5b*; Table S1), suggesting that the consequences of telocyte depletion in embryos (Aoki et al., 2016) and impaired Wnt secretion in adult *Foxl1-Cre;Porcn*^{Ff} mice (Shoshkes-Carmel et al., 2018) may reflect non-canonical functions. scRNA analysis of whole mesenchyme also identified MFs as a second *Foxl1*-expressing cell type that might potentially express *Foxl1-Cre*. Moreover, telocytes suppressed organoid growth in our crypt co-cultures, a finding that pairs with their abundant expression of *Bmp*, compared to *Wnt* or *Rspo* transcripts. In contrast, trophocytes and other PDGFRA^{lo} cells express the canonical ligand *Wnt2b* and three *Rspo* genes. These products explain why trophocytes replace both an RSPO and a BMPi in enteroid cultures, while the CD81⁻ PDGFRA^{lo} cells can substitute for RSPO1. Although we did not evaluate which cells contribute to local Wnt gradients, we observed expression of Wnt antagonists *Sfrp1*, *Frzb*, *Wif1*, and *Dkk2* in PDGFRA⁺ as well as other mesenchymal cells. Thus, among signals that help distinguish ISC from terminally differentiated villus cells, the Wnt network is likely complex and architecturally nuanced. Some evidence even suggests that Wnt3 travels away from an epithelial origin not by diffusion, but by binding to cells that replicate (Farin et al., 2016). We propose that the intestinal BMP gradient follows a simpler logic: polarized restriction of BMPs in telocyte aggregates and of GREM1 in trophocytes.

Ablation of *Grem1*⁺ stromal cells resulted in substantial ISC loss, while TA cells continued to proliferate. These findings imply that ISC uniquely depend on sub-cryptal trophocytes and possibly also on superficial *Grem1*⁺ smooth muscle, while the TA compartment

withstands higher BMP tone. *Grem1* null mice are, however, viable, with ostensibly intact crypt function (Davis et al., 2015). One possibility is that *Grem1* null trophocytes compensate by expressing other BMPi; alternatively, ablation of *Grem1*⁺ cells likely diminishes multiple signals, such as RSPO support for Wnt ligands, and therefore the outcome is more severe than with loss of *Grem1* alone. As *Grem1*^{Cre-ER} mice could not resolve these possibilities *in vivo*, we used crypt co-cultures to delineate trophocyte capacity in the absence of any recombinant factor and of other stromal cells supplemented with specific factors. Beyond the functional assessments *in vivo* and *in vitro*, our conclusions rest on meticulous examination of intestinal mesenchyme by advanced microscopy, coupled with transcriptome analysis of unfractionated mesenchyme and well-defined populations at single-cell resolution. Inspection of whole-mount tissues resolved cell identities and relationships to an unprecedented degree and identified PDGFRA^{lo} cells as a dominant mesenchymal population, distinct from SMA⁺ MFs, NG2⁺ pericytes, CD31⁺ endothelial cells or PDGFRA^{hi} telocytes, and accounting for the largest fraction of resident sub-epithelial cells. The stereotypic arrangement of diverse cells at uniform distances from the epithelium and from each other likely reflects various signaling roles in intestinal homeostasis. These high-resolution anatomic and molecular maps of the mesenchyme provide a foundation for future investigation.

Many prevailing views on stem cell properties originated in studies of bone marrow, where a few hematopoietic stem cells (HSCs) divide infrequently and asymmetrically. The bone marrow niche, now increasingly understood in cellular and molecular terms (Baryawno et al., 2019; Ding et al., 2012; Kunisaki et al., 2013), supports these behaviors in the local tissue context, which lacks distinct landmarks such as crypt units. Importantly, ISC properties differ materially from those of HSCs (Clevers, 2015). Each crypt contains up to a dozen *Lgr5*⁺ cells that replicate symmetrically every 2–4 days (Kozar et al., 2013; Lopez-Garcia et al., 2010; Snippert et al., 2010) and when ISCs are ablated by g-irradiation or other injury, various crypt progenitors quickly dedifferentiate to restore the ISC compartment (Tetteh et al., 2016; Tian et al., 2011; van Es et al., 2012). Unlike bone marrow, the intestinal stroma therefore rapidly senses ISC loss and supports robust replication of stem and progenitor cells, thus helping restore epithelial integrity. Our detailed cellular and molecular delineation of mesenchymal populations sets a stage to ask which cells sense and respond to ISC deficits, and because impaired BMP signaling influences intestinal tumorigenesis (Davis et al., 2015; Jaeger et al., 2012; Cancer Genome Atlas Network, 2012), also whether the native signaling gradient can be exploited to limit excessive ISC activity in tumors. As a start, it will be instructive to know how the native mesenchyme is possibly restructured in cancers.

STAR★METHODS

Detailed methods are provided in the online version of this paper and include the following:

LEAD CONTACT AND MATERIALS AVAILABILITY

Further information and requests for resources and reagents should be directed to and will be fulfilled by the Lead Contact, Ramesh Shivdasani (ramesh_shivdasani@dfci.harvard.edu).

This study did not generate any unique reagents and the *Grem1^{Cre}* mouse line generated in this study is available upon request to Shannon Turley (Genentech, turley.shannon@gene.com) after execution of a Materials Transfer Agreement.

EXPERIMENTAL MODEL AND SUBJECT DETAILS

Mice—*Pdgfra^{H2BeGFP}* mice (Hamilton et al., 2003) were purchased from Jackson Laboratories (stock 007669). *Grem1^{Cre-ER(T2)}* mice were generated by inserting a *Cre^{ER(T2)}* cassette into the second *Grem1* exon (V.N.K. et al., unpublished data) and crossed with both ROSA26^{YFP} (Srinivas et al., 2001) (Jackson Laboratories stock 006148) and *ROSA26^{ΔDTR}* mice (Buch et al., 2005) (Jackson Laboratories stock 007900) to ablate *Grem1⁺* cells. Mice were at least 8 weeks old at the age of experimental treatments and cell isolations. Mice of both sexes were used in all experiments and littermates were used as controls. All animal procedures and experiments were approved and monitored by Animal Care and Use Committees at the Dana-Farber Cancer Institute (wild-type and *Pdgfra^{H2BeGFP}*) or Genentech (*Grem1^{Cre-ER(T2)}*).

METHOD DETAILS

Experimental Design—The number of independent replicates and statistical methods is given in the respective figure legends. No sample size estimations and no blinding were performed. Further information on statistical tests is provided in the respective STAR Methods section.

Mouse treatments—*Grem1^{CreERT2};ROSA26^{ΔDTR}* mice received 4-OH tamoxifen (Sigma-Aldrich, 20 mg/ml) by intra-peritoneal injection for 5 consecutive days to allow recombination at LoxP sites. Between 15 and 25 days later, *Grem1^{CreERT2};ROSA26^{ΔDTR}* mice received intra-peritoneal injections of Diphtheria toxin (Enzo Life Sciences, 25 ng/g weight) on 2 consecutive days and were euthanized for tissue harvest 2, 5, and 8 days after the second dose.

Immunohistochemistry—Whole-mount tissue immunohistochemistry was performed as described (Bernier-Latmani and Petrova, 2016). Mice were perfused with cold phosphate-buffered saline (PBS), followed by 4% paraformaldehyde (PFA). Muscle layers were removed manually and strips of small intestine were pinned onto agarose plates and fixed overnight with 15% picric acid and 0.5% PFA in PBS. In this and all subsequent steps, the tissue was rocked gently. After rinsing in PBS, the tissue was placed in 10%, then 20% sucrose over the span of 1 day, followed by blocking buffer (PBS containing 0.125% BSA, 0.003% Triton X-100, 0.05% donkey serum, and 0.0005% NaN₃) for 6 h and overnight incubation with primary antibodies (Ab). After 5 hourly washes in PBS, tissues were incubated overnight with secondary Ab conjugated with Alexa Fluor (Invitrogen) in buffer containing 4',6-diamidino-2-phenylindole (DAPI), then washed in PBS for 5 h with a change of buffer every 30 min and post-fixed in 4% PFA for 2 days. Cut 1-mm fragments of tissue were then placed on glass slides with spacers (Grace Bio-Labs, 654002), cleared using FocusClear (CelExplorer, FC-101) for 30 min, and VectaShield mounting medium (Vector Laboratories) and a coverslip were applied. Imaging was performed on tissues from at least 3 independent animals to generate representative and comprehensive anatomical resolution.

Routine immunohistochemistry was performed on tissues fixed as described above and placed in OCT compound (Tissue-Tek, VWR Scientific catalog no. 4583) or embedded in paraffin. 7 μ m OCT-sections were prepared using a Leica CM3050 cryostat and paraffin sections were cut on a Leica RM2255 microtome. The following Ab were used: LYVE1 (Angiobio 11–034; RRID: AB_2813732); CD31 (BD 557355; RRID: AB_396660); NG2 (Millipore AB5320; RRID: AB_11213678); Laminin (Sigma L9393; RRID: AB_477163); PDGFRA (1:100, R&D Systems AF1062; RRID: AB_2236897); Alpha-smooth muscle actin (Abcam ab5694; RRID: AB_2223021); TUJ1 (Abcam ab18207; RRID: AB_444319); KI67 (Gentex, GTX16667; RRID: AB_422351); GFP (Abcam ab6662; RRID: AB_305635); PDPN (Biolegend 127410; RRIDs: AB_10613649); Lysozyme (Dako A0099; RRID: AB_2341230); Secondary antibodies (Alexa Fluor, Invitrogen). All antibodies at 1:1000 dilution (unless indicated). *Pdgfra*^{H2BeGFP} mouse sections were viewed on a Leica SP5X laser scanning confocal microscope and *Grem1*^{Dtr} sections on a Leica DM4B microscope. Images and movies were further processed using ImageJ Fiji software (Schindelin et al., 2012). Schematic illustrations were hand-drawn and processed using Adobe Photoshop CC 2018. Figure S1E was generated as a composite of two images overlaid using Microsoft 365 ProPlus Office Powerpoint.

Mesenchymal cell isolation and flow cytometry—Intestinal mesenchyme was isolated similar to previous reports (Kurahashi et al., 2013; Stzepourginski et al., 2015). Small intestines were harvested after perfusing adult wild-type or *Pdgfra*^{H2BeGFP} mice (Hamilton et al., 2003) with ice-cold PBS. Outer muscle layers were stripped manually using fine tweezers and the epithelium was denuded by shaking the tissue in pre-warmed Hank's Balanced Salt Solution (HBSS, Life Technologies) containing 10 mM EDTA for 20 min at 37°C. The remaining tissue was rinsed with PBS, minced using a scalpel, and digested by rotating at 37°C in 1.5 mg/ml collagenase II (Worthington, LS004176) diluted in Dulbecco's Modified Eagle Medium (DMEM) containing 5% fetal bovine serum (FBS). The tissue suspension was passed through a pipette gently every 10 min, cells were extracted 3 times every 20 min, and the enzyme solution was replaced at each harvest. Extracted cells were centrifuged at 500 *g* for 5 min, washed with PBS containing 2 mM EDTA and 2% FBS (FACS buffer), and resuspended in the same buffer for Ab staining. To isolate CD31⁺ vascular (LYVE1⁻) and lymphatic (LYVE1⁻) endothelial cells, LYVE1 Ab (1:100, AngioBio 11–034; RRID: AB_2813732) was applied for 30 min and cells were washed in FACS buffer, followed by further staining with FITC-conjugated anti-rabbit IgG (1:1000, Jackson ImmunoResearch 2337972) and APC-conjugated CD31 Ab (1:100, BD Biosciences 551262; RRID: AB_398497). *Grem1*^{Cre}; *Ros26*^{YFP/iDtr} mouse ilea were incubated in a chelation buffer (RPMI with 5 mM EDTA) with shaking for 40 min, vortexed gently, and washed to remove epithelium. The mesenchyme was digested in a solution containing 5 mg/ml DNaseI and 100 U/ml Collagenase VIII for 1 h at 37°C with shaking. The material was then passed through a pipet 5 times, strained, stained with PDPN (1:200, Biolegend 127412; RRID: AB_10613648) and PDGFRA (1:200, Invitrogen 12–1401-81; RRID: AB_657615) Ab, and analyzed in a BD Fortessa or Aria instrument. CD81⁺ and CD81⁻ mesenchymal PDGFRA^{lo} cell fractions were isolated from *Pdgfra*^{H2BeGFP} mouse intestines. CD81 Ab (1:100, Invitrogen 13–0811-81; RRID: AB_466514) and PDGFRA Ab (1:100, Invitrogen 13–1401-80; RRID: AB_466606) was applied for 30 min, followed by washing and staining

with APC-conjugated streptavidin (Invitrogen, 17–4317-82). Cells were detected and sorted on a Sony SH800z flow cytometer, with gating against DAPI to identify live cells.

In situ RNA hybridization—mRNAs were localized in specific cells by the RNAscope (Advanced Cell Diagnostics) method (Wang et al., 2012a) on intestines collected from at least 3, and up to 4, different animals. Advanced Cell Diagnostics designed probe sets for *Grem1*, *Bmp5*, *Bmp7*, *Lgr5*, and *Olfm4*. After the hybridization protocol, which destroys GFP fluorescence, GFP signals were revealed by immunohistochemistry. Slides were washed for 5 min in PBS containing 0.1% Tween-20, blocked for 1 hr at room temperature in PBS containing 5% NGS, and exposed overnight at 4°C to GFP Ab (1:100, Abcam ab6556; RRID: AB_305564). After multiple 5-min washes in PBS and 90-min incubation with secondary Ab (AlexaFluor, Invitrogen) at room temperature, DAPI was applied and slides were mounted according to the RNAscope protocol. *Grem1*, *Bmp5*, and *Bmp7* images in *Pdgfra^{H2BeGFP}* mice were obtained on a Leica SP5X laser scanning confocal microscope; *Grem1*, *Lgr5*, *Id1*, *Axin2*, and *Olfm4* images in *Grem1^{Dtr}* mice were obtained on a Zeiss Axioskop 40 microscope.

In vitro co-cultures—Unfractionated mesenchyme extracted from *Pdgfra^{H2BeGFP}* mice was plated on non-pyrogenic, gas plasma surface treated polystyrene tissue culture plates (Falcon) in DMEM and F12 medium (GIBCO, 12634–010) supplemented with 10% FBS (Corning, 35–010-CV), penicillin, streptomycin, Glutamax, and HEPES buffer (Basal media + FBS). The medium was replaced 24 h after plating; 5 to 7 days later, cells were removed using 1X TrypLE Express (GIBCO, 15 min at 37°C), washed in FACS buffer, and stained with CD81 Ab for flow cytometry as described above. To determine the stability of molecular signatures in these short-term cultures, we performed qRT-PCR on 3 different samples of GFP^{hi} telocytes and CD81⁺ and CD81⁻ PDGFRA^{lo} cells. mRNA expression values were quantified relative to *Gapdh* (2^{-DCT}).

Crypt epithelium was isolated and passaged as described (Sato and Clevers, 2013). For co-cultures, ~100 crypts were cultured in 24-well tissue culture plates loaded with 20 mL drops of Matrigel (Corning) or type I rat tail collagen (First Link, UK) together with 4×10⁴ mesenchymal cells sorted by flow cytometry, after short-term culture as described above, and recombinant EGF (Thermo Fisher, 50 ng/mL). Basal Media (described above) was supplemented with either Noggin (Peprotech, 100 ng/mL), Rspo1 (cell culture supernatant from 293T-HA-Rspo1-Fc cells, 1 ug/mL), both, or Gremlin1 (Thermo Fisher, 2 ug/ul). Colonies were imaged using an Evos FL microscope (Thermo Scientific).

QUANTIFICATION AND STATISTICAL ANALYSIS

Quantitation of GFP signals—GFP^{hi} signals were quantified by inputting confocal microscopy image z stacks into MATLAB (The Mathworks Inc.) as monochrome single-image series for the DAPI and green fluorescence (GFP) channels. The serosa was identified in valid z-slices and vectors parallel to the crypt-villus axis were defined along the serosal surface to quantify the distribution of the GFP signal along a total of 137 crypts and 53 villi from 3 independent animals. The signal threshold allowed only GFP^{hi} cells to register in this quantitation.

Quantitation of co-culture assays—Organoid (spheroid) structures were counted with a Nikon Eclipse TS100 microscope 6 days after co-culture (P0) or 3 days after the first passage (P1). Graphs and associated statistics were generated using GraphPad Prism v7.03.

Computational analysis for RNA sequencing—Cell populations, isolated as described above, were placed in Trizol Reagent (ThermoFisher) and RNA was purified using the RNeasy Microkit (QIAGEN). Total RNA (5–10ng) was used to prepare libraries with the SMART-Seq v4 Ultra Low Input RNA kit (Clontech) and libraries were sequenced on a NextSeq500 instrument (Illumina) to obtain 75-bp single-end reads. Data were analyzed using the VIPER pipeline with default settings (Cornwell et al., 2018) and aligned to mouse reference genome mm10 using the STAR aligner (Dobin et al., 2013). RPKM (reads per kilobase per million) values were generated from STAR counts, data quality was verified using RSeQC (Wang et al., 2012b), and further statistical analyses occurred on the R platform (R Development Core Team, 2013). Data were normalized and differential gene expression ($P_{adj} < 0.05$, absolute \log_2 fold-change > 1.5) was determined in the DESeq2 package (Love et al., 2014). Pearson correlation coefficients were calculated from DESeq2 normalized counts and plotted using the Corrplot package (Wei et al., 2017) in R. Relationship among samples was also assessed by principal component analysis (PCA) of DESeq2 rlog-transformed counts (Love et al., 2014) and the expression heatmap (Figure 2A) was generated using Morpheus (Broad Institute). To generate the Integrative Genome Viewer Tracks (Figure 2A), we generated RPKM-normalized bigwigs using the bamCoverage tool from the DeepTools package (Ramírez et al., 2016) and loaded into IGV v2.3 (Broad Institute). Epithelial cell mRNA data were published previously (Jadhav et al., 2017) and are available in Gene Expression Omnibus series GSE83394 and GSE71713 (Libraries - Lgr5⁺ ISC: GSM2201132 and GSM2201133, Paneth cells: GSM2201146 and GSM2201148, crypt enterocyte progenitors: GSM2201137 and GSM2201138, unfractionated villus epithelium: GSM1843521 and GSM1843522).

For scRNA sequencing, PDGFRA^{hi} and PDGFRA^{lo} cells were isolated by flow cytometry at a ratio of 1:2 from a male *Pdgfra*^{H2BeGFP} mouse. Using the Single Cell 3⁰ V2 assay, we loaded 8,700 cells onto a Chromium Controller (10x Genomics). Reverse transcription, cDNA amplification, and library preparation were completed according to the manufacturer's recommendations. scRNA libraries were sequenced on a HiSeq4000 instrument (Illumina).

Computational analysis for scRNA-seq

Pre-processing: Libraries were de-multiplexed, aligned to the mm10 mouse transcriptome, and unique molecular identifiers (UMIs) were counted using Cell Ranger (10X Genomics) v2.1.1 for PDGFRA⁺ cells (Figure 3) and v3.1.1 for unfractionated mesenchyme (Figure 4). Data were analyzed using the Seurat package v2.3.3 in R. PDGFRA⁺ cells with 1,500 detected transcripts and genes expressed in 100 single cells were retained, resulting in 9,334 detectable genes in 2,894 single cells (Figure 3). Further exclusion of cells with $> 3\%$ mitochondrial transcripts gave a final count of 2,595 informative single cells. Data were normalized and log-transformed using the “LogNormalize” function in Seurat. For unfractionated mesenchyme, we enhanced cell-sequencing depth by generating and then

merging two separate libraries. Cells with 1,500 transcripts and < 10% mitochondrial transcripts were retained (total 9,353 cells – Figure S4). We removed all clusters showing *Cd45* (*Ptprc*) expression, other than one small *Pdgfra*-expressing cluster. This left a total of 3,763 resident sub-epithelial stromal cells (Figure S4). Clusters were assigned to known cell types by signature markers using the “FindAllMarkers” function in Seurat, with parameters: *min.pct* 0.25 and *logfc.threshold* 0.25. Markers were then queried using known mouse colon mesenchymal cell-specific genes (Kinchen et al., 2018).

Dimensionality reduction and clustering: For PDGFRA⁺ cells, we selected the top 714 variable genes using the “FindVariableGenes” function in Seurat using parameters: *x.low.cutoff* 0.0125, *x.high.cutoff* 3, and *y.cutoff* 1 for principal component analysis. The top 7 principal components were selected for PDGFRA⁺ cells and top 10 principal components for whole mesenchyme, based on the Jackstraw approach implemented in Seurat ($p < 1e^{-50}$) and visualized using the Barnes–Hut approximate version of t-distributed Stochastic Neighbor Embedding (t-SNE) algorithm (van der Maaten, 2014). We then identified clusters using the “FindClusters” function in Seurat, which implements an algorithm based on optimization nearest-neighbor modularity, using the parameter resolution 0.2 for PDGFRA⁺ cells and 0.4 for unfractionated mesenchyme. This approach identified 3 distinct *Pdgfra*⁺ clusters which were overlaid on the t-SNE plot from PDGFRA⁺ cell scRNA. Marker genes for each cluster were identified using the MAST algorithm (Finak et al., 2015). The correlation heatmap (Figure 3B) was generated using the Spearman correlation of all PDGFRA⁺ cells across the top 7 principal components. After clustering cells from whole mesenchyme, those expressing *Cd34* and *Pdgfra*, but lacking *Cd81* were designated as Lo-2 in the final group of 10 clusters (Figure S4).

Supplementary Material

Refer to Web version on PubMed Central for supplementary material.

ACKNOWLEDGMENTS

We thank J. Bernier-Latmani and T. Petrova for valuable advice on whole-mount tissue processing; D. Hansen and L. Li for helpful discussions on mesenchymal cell isolation; members of the ISC Consortium and D. Kaplan laboratory for critical feedback; and D. Breault and the Harvard Digestive Diseases Center (P30DK034854) organoid facility for reagents, advice, and photomicrography. This work was supported by US National Institutes of Health grants U01DK103152 (Intestinal Stem Cell Consortium of the NIDDK and NIAID), R01DK121540 (to R.A.S.), and R01HG009663 (to G.-C.Y.); fellowships T32EB016652 (Training in Organ Design and Engineering) and F32DK118862 (to N.M.); and gifts from the Lind family.

REFERENCES

- Aoki R, Shoshkes-Carmel M, Gao N, Shin S, May CL, Golson ML, Zahm AM, Ray M, Wiser CL, Wright CV, and Kaestner KH (2016). Foxl1-expressing mesenchymal cells constitute the intestinal stem cell niche. *Cell. Mol. Gastroenterol. Hepatol* 2, 175–188. [PubMed: 26949732]
- Aono A, Hazama M, Notoya K, Taketomi S, Yamasaki H, Tsukuda R, Sasaki S, and Fujisawa Y. (1995). Potent ectopic bone-inducing activity of bone morphogenetic protein-4/7 heterodimer. *Biochem. Biophys. Res. Commun* 210, 670–677. [PubMed: 7763240]
- Barkai N, and Shilo BZ (2009). Robust generation and decoding of morphogen gradients. *Cold Spring Harb. Perspect. Biol* 1, a001990.

- Baryawno N, Przybylski D, Kowalczyk MS, Kfoury Y, Severe N, Gustafsson K, Kokkaliaris KD, Mercier F, Tabaka M, Hofree M, et al. (2019). A cellular taxonomy of the bone marrow stroma in homeostasis and leukemia. *Cell* 177, 1915–1932. [PubMed: 31130381]
- Batts LE, Polk DB, Dubois RN, and Kulesa H. (2006). Bmp signaling is required for intestinal growth and morphogenesis. *Dev. Dyn* 235, 1563–1570. [PubMed: 16538672]
- Bernier-Latmani J, and Petrova TV (2016). High-resolution 3D analysis of mouse small-intestinal stroma. *Nat. Protoc* 11, 1617–1629. [PubMed: 27560169]
- Bernier-Latmani J, Cisarovsky C, Demir CS, Bruand M, Jaquet M, Davanture S, Ragusa S, Siegert S, Dormond O, Benedito R, et al. (2015). DLL4 promotes continuous adult intestinal lacteal regeneration and dietary fat transport. *J. Clin. Invest* 125, 4572–4586. [PubMed: 26529256]
- Buch T, Heppner FL, Tertilt C, Heinen TJ, Kremer M, Wunderlich FT, Jung S, and Waisman A. (2005). A Cre-inducible diphtheria toxin receptor mediates cell lineage ablation after toxin administration. *Nat. Methods* 2, 419–426. [PubMed: 15908920]
- Butler A, Hoffman P, Smibert P, Papalexi E, and Satija R. (2018). Integrating single-cell transcriptomic data across different conditions, technologies, and species. *Nat Biotechnol* 36, 411–420. [PubMed: 29608179]
- Cancer Genome Atlas Network (2012). Comprehensive molecular characterization of human colon and rectal cancer. *Nature* 487, 330–337. [PubMed: 22810696]
- Chen L, Toke NH, Luo S, Vasoya RP, Fullem RL, Parthasarathy A, Perekatt AO, and Verzi MP (2019). A reinforcing HNF4-SMAD4 feed-forward module stabilizes enterocyte identity. *Nat. Genet* 51, 777–785. [PubMed: 30988513]
- Clevers H. (2013). The intestinal crypt, a prototype stem cell compartment. *Cell* 154, 274–284. [PubMed: 23870119]
- Clevers H. (2015). STEM CELLS. What is an adult stem cell? *Science* 350, 1319–1320. [PubMed: 26659043]
- Cornwell M, Vangala M, Taing L, Herbert Z, Köster, J., Li, B., Sun, H., Li, T., Zhang, J., Qiu, X., et al. (2018). VIPER: Visualization Pipeline for RNA-seq, a Snakemake workflow for efficient and complete RNA-seq analysis. *BMC Bioinformatics* 19, 135. [PubMed: 29649993]
- Davis H, Irshad S, Bansal M, Rafferty H, Boitsova T, Bardella C, Jaeger E, Lewis A, Freeman-Mills L, Giner FC, et al. (2015). Aberrant epithelial GREM1 expression initiates colonic tumorigenesis from cells outside the stem cell niche. *Nat. Med* 21, 62–70. [PubMed: 25419707]
- Degirmenci B, Valenta T, Dimitrieva S, Hausmann G, and Basler K. (2018). GLI1-expressing mesenchymal cells form the essential Wnt-secreting niche for colon stem cells. *Nature* 558, 449–453. [PubMed: 29875413]
- Ding L, Saunders TL, Enikolopov G, and Morrison SJ (2012). Endothelial and perivascular cells maintain haematopoietic stem cells. *Nature* 481, 457–462. [PubMed: 22281595]
- Dobin A, Davis CA, Schlesinger F, Drenkow J, Zaleski C, Jha S, Batut P, Chaisson M, and Gingeras TR (2013). STAR: ultrafast universal RNA-seq aligner. *Bioinformatics* 29, 15–21. [PubMed: 23104886]
- Farin HF, Van Es JH, and Clevers H. (2012). Redundant sources of Wnt regulate intestinal stem cells and promote formation of Paneth cells. *Gastroenterology* 143, 1518–1529. [PubMed: 22922422]
- Farin HF, Jordens I, Mosa MH, Basak O, Korving J, Tauriello DV, de Punder K, Angers S, Peters PJ, Maurice MM, and Clevers H. (2016). Visualization of a short-range Wnt gradient in the intestinal stem-cell niche. *Nature* 530, 340–343. [PubMed: 26863187]
- Fearon ER, and Vogelstein B. (1990). A genetic model for colorectal tumorigenesis. *Cell* 61, 759–767. [PubMed: 2188735]
- Finak G, McDavid A, Yajima M, Deng J, Gersuk V, Shalek AK, Slichter CK, Miller HW, McElrath MJ, Prlic M, et al. (2015). MAST: a flexible statistical framework for assessing transcriptional changes and characterizing heterogeneity in single-cell RNA sequencing data. *Genome Biol.* 16, 278. [PubMed: 26653891]
- Gregorieff A, Pinto D, Begthel H, Destrée O, Kielman M, and Clevers H. (2005). Expression pattern of Wnt signaling components in the adult intestine. *Gastroenterology* 129, 626–638. [PubMed: 16083717]

- Greicius G, Kabiri Z, Sigmundsson K, Liang C, Bunte R, Singh MK, and Virshup DM (2018). PDGFRa⁺ pericyptal stromal cells are the critical source of Wnts and RSPO3 for murine intestinal stem cells in vivo. *Proc. Natl. Acad. Sci. USA* 115, E3173–E3181.
- Hamilton TG, Klinghoffer RA, Corrin PD, and Soriano P. (2003). Evolutionary divergence of platelet-derived growth factor alpha receptor signaling mechanisms. *Mol. Cell. Biol* 23, 4013–4025. [PubMed: 12748302]
- Haramis AP, Begthel H, van den Born M, van Es J, Jonkheer S, Offerhaus GJ, and Clevers H. (2004). De novo crypt formation and juvenile polyposis on BMP inhibition in mouse intestine. *Science* 303, 1684–1686. [PubMed: 15017003]
- He XC, Zhang J, Tong WG, Tawfik O, Ross J, Scoville DH, Tian Q, Zeng X, He X, Wiedemann LM, et al. (2004). BMP signaling inhibits intestinal stem cell self-renewal through suppression of Wnt-beta-catenin signaling. *Nat. Genet* 36, 1117–1121. [PubMed: 15378062]
- Jadhav U, Saxena M, O'Neill NK, Saadatpour A, Yuan GC, Herbert Z, Murata K, and Shivdasani RA (2017). Dynamic reorganization of chromatin accessibility signatures during dedifferentiation of secretory precursors into Lgr5⁺ intestinal stem cells. *Cell Stem Cell* 21, 65–77. [PubMed: 28648363]
- Jaeger E, Leedham S, Lewis A, Segditsas S, Becker M, Cuadrado PR, Davis H, Kaur K, Heinimann K, Howarth K, et al.: HMPS Collaboration (2012). Hereditary mixed polyposis syndrome is caused by a 40-kb upstream duplication that leads to increased and ectopic expression of the BMP antagonist GREM1. *Nat. Genet* 44, 699–703. [PubMed: 22561515]
- Kabiri Z, Greicius G, Madan B, Biechele S, Zhong Z, Zaribafzadeh H, Edison, Aliyev J, Wu Y, Bunte R, et al. (2014). Stroma provides an intestinal stem cell niche in the absence of epithelial Wnts. *Development* 141, 2206–2215. [PubMed: 24821987]
- Kaito T, Morimoto T, Mori Y, Kanayama S, Makino T, Takenaka S, Sakai Y, Otsuru S, Yoshioka Y, and Yoshikawa H. (2018). BMP-2/7 heterodimer strongly induces bone regeneration in the absence of increased soft tissue inflammation. *Spine J.* 18, 139–146. [PubMed: 28735764]
- Kim KA, Kakitani M, Zhao J, Oshima T, Tang T, Binnerts M, Liu Y, Boyle B, Park E, Emtage P, et al. (2005). Mitogenic influence of human R-spondin1 on the intestinal epithelium. *Science* 309, 1256–1259. [PubMed: 16109882]
- Kim HS, Neugebauer J, McKnite A, Tilak A, and Christian JL (2019). BMP7 functions predominantly as a heterodimer with BMP2 or BMP4 during mammalian embryogenesis. *eLife* 8, e48872.
- Kinchen J, Chen HH, Parikh K, Antanaviciute A, Jagielowicz M, Fawcner-Corbett D, Ashley N, Cubitt L, Mellado-Gomez E, Attar M, et al. (2018). Structural remodeling of the human colonic mesenchyme in inflammatory bowel disease. *Cell* 175, 372–386. [PubMed: 30270042]
- Kosinski C, Li VS, Chan AS, Zhang J, Ho C, Tsui WY, Chan TL, Mifflin RC, Powell DW, Yuen ST, et al. (2007). Gene expression patterns of human colon tops and basal crypts and BMP antagonists as intestinal stem cell niche factors. *Proc. Natl. Acad. Sci. USA* 104, 15418–15423.
- Kozar S, Morrissey E, Nicholson AM, van der Heijden M, Zecchini HI, Kemp R, Tavaré S, Vermeulen L, and Winton DJ (2013). Continuous clonal labeling reveals small numbers of functional stem cells in intestinal crypts and adenomas. *Cell Stem Cell* 13, 626–633. [PubMed: 24035355]
- Kuhnert F, Davis CR, Wang HT, Chu P, Lee M, Yuan J, Nusse R, and Kuo CJ (2004). Essential requirement for Wnt signaling in proliferation of adult small intestine and colon revealed by adenoviral expression of Dickkopf-1. *Proc. Natl. Acad. Sci. USA* 101, 266–271. [PubMed: 14695885]
- Kunisaki Y, Bruns I, Scheiermann C, Ahmed J, Pinho S, Zhang D, Mizoguchi T, Wei Q, Lucas D, Ito K, et al. (2013). Arteriolar niches maintain haematopoietic stem cell quiescence. *Nature* 502, 637–643. [PubMed: 24107994]
- Kurahashi M, Nakano Y, Hennig GW, Ward SM, and Sanders KM (2012). Platelet-derived growth factor receptor a-positive cells in the tunica muscularis of human colon. *J. Cell. Mol. Med* 16, 1397–1404. [PubMed: 22225616]
- Kurahashi M, Nakano Y, Peri LE, Townsend JB, Ward SM, and Sanders KM (2013). A novel population of subepithelial platelet-derived growth factor receptor a-positive cells in the mouse and human colon. *Am. J. Physiol. Gastrointest. Liver Physiol* 304, G823–G834. [PubMed: 23429582]

- Lopez-Garcia C, Klein AM, Simons BD, and Winton DJ (2010). Intestinal stem cell replacement follows a pattern of neutral drift. *Science* 330, 822–825. [PubMed: 20929733]
- Love MI, Huber W, and Anders S. (2014). Moderated estimation of fold change and dispersion for RNA-seq data with DESeq2. *Genome Biol.* 15, 550. [PubMed: 25516281]
- Ogasawara R, Hashimoto D, Kimura S, Hayase E, Ara T, Takahashi S, Ohigashi H, Yoshioka K, Tateno T, Yokoyama E, et al. (2018). Intestinal lymphatic endothelial cells produce R-Spondin3. *Sci. Rep* 8, 10719.
- Ogata T, Wozney JM, Benezra R, and Noda M. (1993). Bone morphogenetic protein 2 transiently enhances expression of a gene, *Id* (inhibitor of differentiation), encoding a helix-loop-helix molecule in osteoblast-like cells. *Proc. Natl. Acad. Sci. USA* 90, 9219–9222. [PubMed: 8415680]
- Pinto D, Gregorieff A, Begthel H, and Clevers H. (2003). Canonical Wnt signals are essential for homeostasis of the intestinal epithelium. *Genes Dev.* 17, 1709–1713. [PubMed: 12865297]
- Potten CS (1998). Stem cells in gastrointestinal epithelium: numbers, characteristics and death. *Philos. Trans. R. Soc. Lond. B Biol. Sci* 353, 821–830. [PubMed: 9684279]
- Powell DW, Pinchuk IV, Saada JI, Chen X, and Mifflin RC (2011). Mesenchymal cells of the intestinal lamina propria. *Annu. Rev. Physiol* 73, 213–237. [PubMed: 21054163]
- Ramírez F, Ryan DP, Grüning B, Bhardwaj V, Kilpert F, Richter AS, Heyne S, Dündar F, and Manke T. (2016). deepTools2: a next generation web server for deep-sequencing data analysis. *Nucleic Acids Res.* 44 (W1), W160–5. [PubMed: 27079975]
- Qi Z, Li Y, Zhao B, Xu C, Liu Y, Li H, Zhang B, Wang X, Yang X, Xie W, et al. (2017). BMP restricts stemness of intestinal Lgr5(+) stem cells by directly suppressing their signature genes. *Nat Commun* 8, 13824.
- R Development Core Team (2013). R: A language and environment for statistical computing (R Foundation for Statistical Computing).
- Robinson JT, Thorvaldsdottir H, Winckler W, Guttman M, Lander ES, Getz G, and Mesirov JP (2011). Integrative genomics viewer. *Nat Biotechnol* 29, 24–26. [PubMed: 21221095]
- Roulis M, and Flavell RA (2016). Fibroblasts and myofibroblasts of the intestinal lamina propria in physiology and disease. *Differentiation* 92, 116–131. [PubMed: 27165847]
- Sailaja BS, He XC, and Li L. (2016). The regulatory niche of intestinal stem cells. *J. Physiol* 594, 4827–4836. [PubMed: 27060879]
- Sato T, and Clevers H. (2013). Primary mouse small intestinal epithelial cell cultures. *Methods Mol. Biol* 945, 319–328. [PubMed: 23097115]
- Sato T, Vries RG, Snippert HJ, van de Wetering M, Barker N, Stange DE, van Es JH, Abo A, Kujala P, Peters PJ, and Clevers H. (2009). Single Lgr5 stem cells build crypt-villus structures in vitro without a mesenchymal niche. *Nature* 459, 262–265. [PubMed: 19329995]
- Schindelin J, Arganda-Carreras I, Frise E, Kaynig V, Longair M, Pietzsch T, Preibisch S, Rueden C, Saalfeld S, Schmid B, et al. (2012). Fiji: an open-source platform for biological-image analysis. *Nat. Methods* 9, 676–682. [PubMed: 22743772]
- Shen Q, Goderie SK, Jin L, Karanth N, Sun Y, Abramova N, Vincent P, Pumiglia K, and Temple S. (2004). Endothelial cells stimulate self-renewal and expand neurogenesis of neural stem cells. *Science* 304, 1338–1340. [PubMed: 15060285]
- Shoshkes-Carmel M, Wang YJ, Wangenstein KJ, Tóth B, Kondo A, Massasa EE, Itzkovitz S, and Kaestner KH (2018). Subepithelial telocytes are an important source of Wnts that supports intestinal crypts. *Nature* 557, 242–246. [PubMed: 29720649]
- Snippert HJ, van der Flier LG, Sato T, van Es JH, van den Born M, Kroon-Veenboer C, Barker N, Klein AM, van Rheenen J, Simons BD, and Clevers H. (2010). Intestinal crypt homeostasis results from neutral competition between symmetrically dividing Lgr5 stem cells. *Cell* 143, 134–144. [PubMed: 20887898]
- Srinivas S, Watanabe T, Lin CS, William CM, Tanabe Y, Jessell TM, and Costantini F. (2001). Cre reporter strains produced by targeted insertion of EYFP and ECFP into the ROSA26 locus. *BMC Dev. Biol* 1, 4. [PubMed: 11299042]
- Stzepourginski I, Eberl G, and Peduto L. (2015). An optimized protocol for isolating lymphoid stromal cells from the intestinal lamina propria. *J. Immunol. Methods* 421, 14–19. [PubMed: 25599879]

- Stzepourginski I, Nigro G, Jacob JM, Dulauroy S, Sansonetti PJ, Eberl G, and Peduto L. (2017). CD34+ mesenchymal cells are a major component of the intestinal stem cells niche at homeostasis and after injury. *Proc. Natl. Acad. Sci. USA* 114, E506–E513. [PubMed: 28074039]
- Tetteh PW, Basak O, Farin HF, Wiebrands K, Kretzschmar K, Begthel H, van den Born M, Korving J, de Sauvage F, van Es JH, et al. (2016). Replacement of lost Lgr5-positive stem cells through plasticity of their enterocyte-lineage daughters. *Cell Stem Cell* 18, 203–213. [PubMed: 26831517]
- Tian H, Biehs B, Warming S, Leong KG, Rangell L, Klein OD, and de Sauvage FJ (2011). A reserve stem cell population in small intestine renders Lgr5-positive cells dispensable. *Nature* 478, 255–259. [PubMed: 21927002]
- Valdimarsdottir G, Goumans MJ, Rosendahl A, Brugman M, Itoh S, Lebrin F, Sideras P, and ten Dijke P. (2002). Stimulation of Id1 expression by bone morphogenetic protein is sufficient and necessary for bone morphogenetic protein-induced activation of endothelial cells. *Circulation* 106, 2263–2270. [PubMed: 12390958]
- van der Maaten L. (2014). Accelerating t-SNE using tree-based algorithms. *J. Mach. Learn. Res* 15, 3221–3245.
- van Es JH, Sato T, van de Wetering M, Lyubimova A, Yee Nee AN, Gregorieff A, Sasaki N, Zeinstra L, van den Born M, Korving J, et al. (2012). Dll1+ secretory progenitor cells revert to stem cells upon crypt damage. *Nat. Cell Biol* 14, 1099–1104. [PubMed: 23000963]
- Wang F, Flanagan J, Su N, Wang LC, Bui S, Nielson A, Wu X, Vo HT, Ma XJ, and Luo Y. (2012a). RNAscope: a novel in situ RNA analysis platform for formalin-fixed, paraffin-embedded tissues. *J. Mol. Diagn* 14, 22–29. [PubMed: 22166544]
- Wang L, Wang S, and Li W. (2012b). RSeQC: quality control of RNA-seq experiments. *Bioinformatics* 28, 2184–2185. [PubMed: 22743226]
- Wei T, Simko V, Levy M, Xie Y, Jin Y, and Zemla J. (2017). R package “corrplot”: Visualization of a correlation matrix (version 0.84). <https://github.com/taiyun/corrplot>.
- Wolpert L. (1971). Positional information and pattern formation. *Curr. Top. Dev. Biol* 6, 183–224. [PubMed: 4950136]
- Worthley DL, Churchill M, Compton JT, Tailor Y, Rao M, Si Y, Levin D, Schwartz MG, Uygur A, Hayakawa Y, et al. (2015). Gremlin 1 identifies a skeletal stem cell with bone, cartilage, and reticular stromal potential. *Cell* 160, 269–284. [PubMed: 25594183]
- Yoshida S, Sukeno M, and Nabeshima Y. (2007). A vasculature-associated niche for undifferentiated spermatogonia in the mouse testis. *Science* 317, 1722–1726. [PubMed: 17823316]

Highlights

- PDGFRA⁺ stromal cells express trophic factors implicated in intestinal self-renewal
- PDGFRA marks distinct intestinal cells: telocytes, CD81[−] stromal cells, trophocytes
- Villus-dominant telocytes express BMPs; PDGFRA^{lo} trophocytes express *Grem1*
- CD81⁺ trophocytes sustain ISC *in vivo* and alone promote ISC expansion *in vitro*

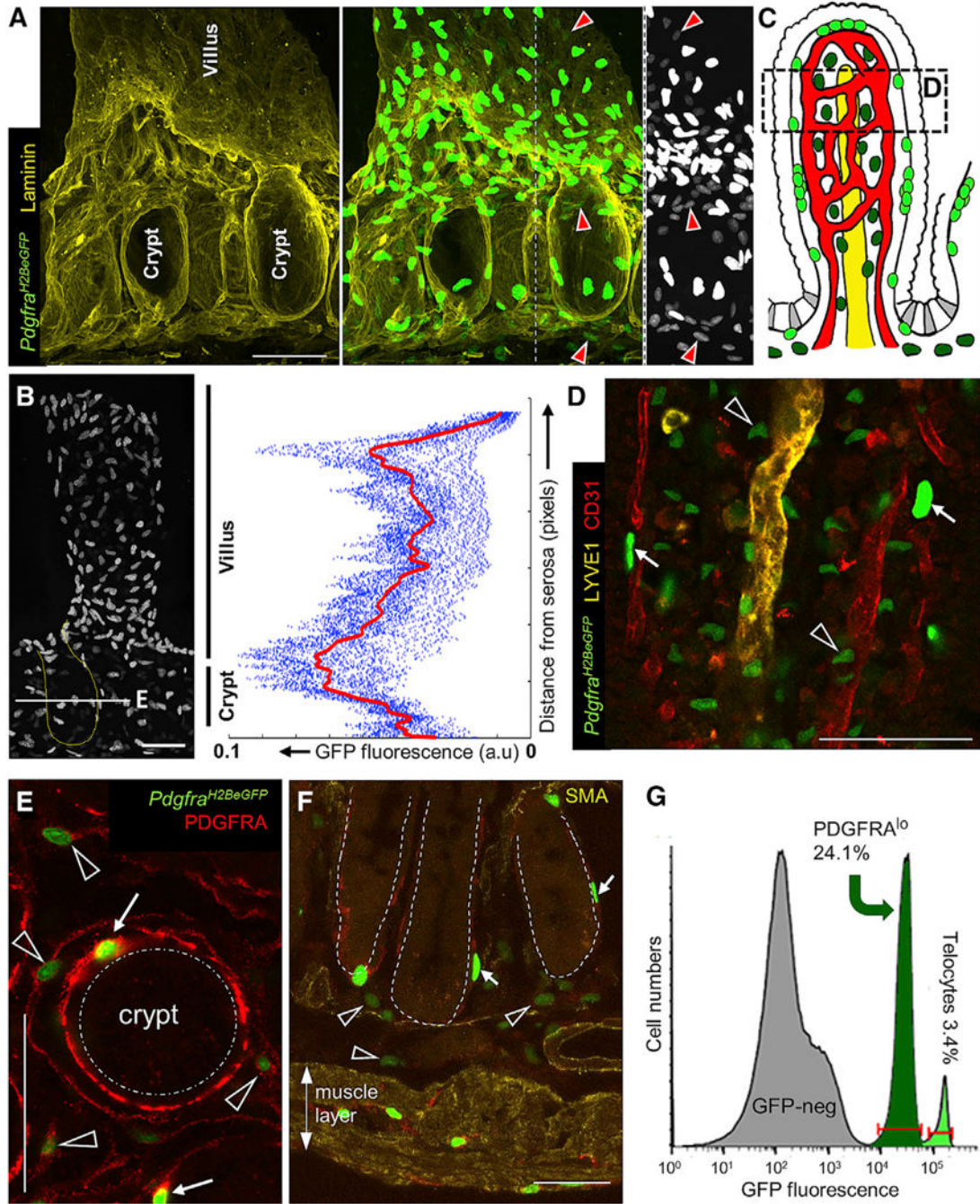


Figure 1. Anatomically and Molecularly Distinct PDGFRA⁺ Populations in Small Intestine Mesenchyme

(A) 3D-rendered image of representative intestinal crypts in *Pdgfra*^{H2BeGFP} mice (left: laminin immunostain, right: laminin + GFP, far right: single crypt showing only GFP in grayscale). Telocytes with bright nuclear fluorescence concentrate at the crypt-villus junction; a separate population of *Pdgfra*^{lo} cells (red arrowheads) is best appreciated in the grayscale image on the far right.

(B) Single crypt-villus unit (crypt outline dotted), showing non-uniform telocyte abundance along the vertical axis. Right: GFP^{hi} signals quantified along crypt-villus units. Dots

represent the signal quantified along each unit; the red line represents the mean signal. The white line in the micrograph indicates the level represented in (E).

(C) Telocyte (neon green) and PDGFRA^{lo} cell (bottle green) distributions illustrated in relation to blood (red) and lymphatic (yellow) vessels, epithelium (white), and Lgr5⁺ ISC (gray). The region represented in (D) is boxed.

(D) 3D-rendered image of telocyte (arrows) and PDGFRA^{lo} cell (arrowheads) positions along the villus radial axis, shown over a region represented by the box in (C). Telocytes are apposed to the epithelium, whereas PDGFRA^{lo} cell lie deeper, intermingled with capillaries.

(E) Crypt cross-section (approximate level marked by the line in B), showing relative positions, PDGFRA expression levels, and cytoplasmic sweep of telocytes (arrows) and PDGFRA^{lo} cells (arrowheads).

(F) PDGFRA^{lo} cells (arrowheads) are present below crypts (dotted outlines), in the submucosa; PDGFRA^{hi} cells (arrows) include telocytes and other cells in the muscularis, as described previously (Kurahashi et al., 2012; Shoshkes-Carmel et al., 2018). All scale bars, 50 μ m.

(G) GFP flow cytometry separates telocytes from the larger population of PDGFRA^{lo} cells. See also Figure S1.

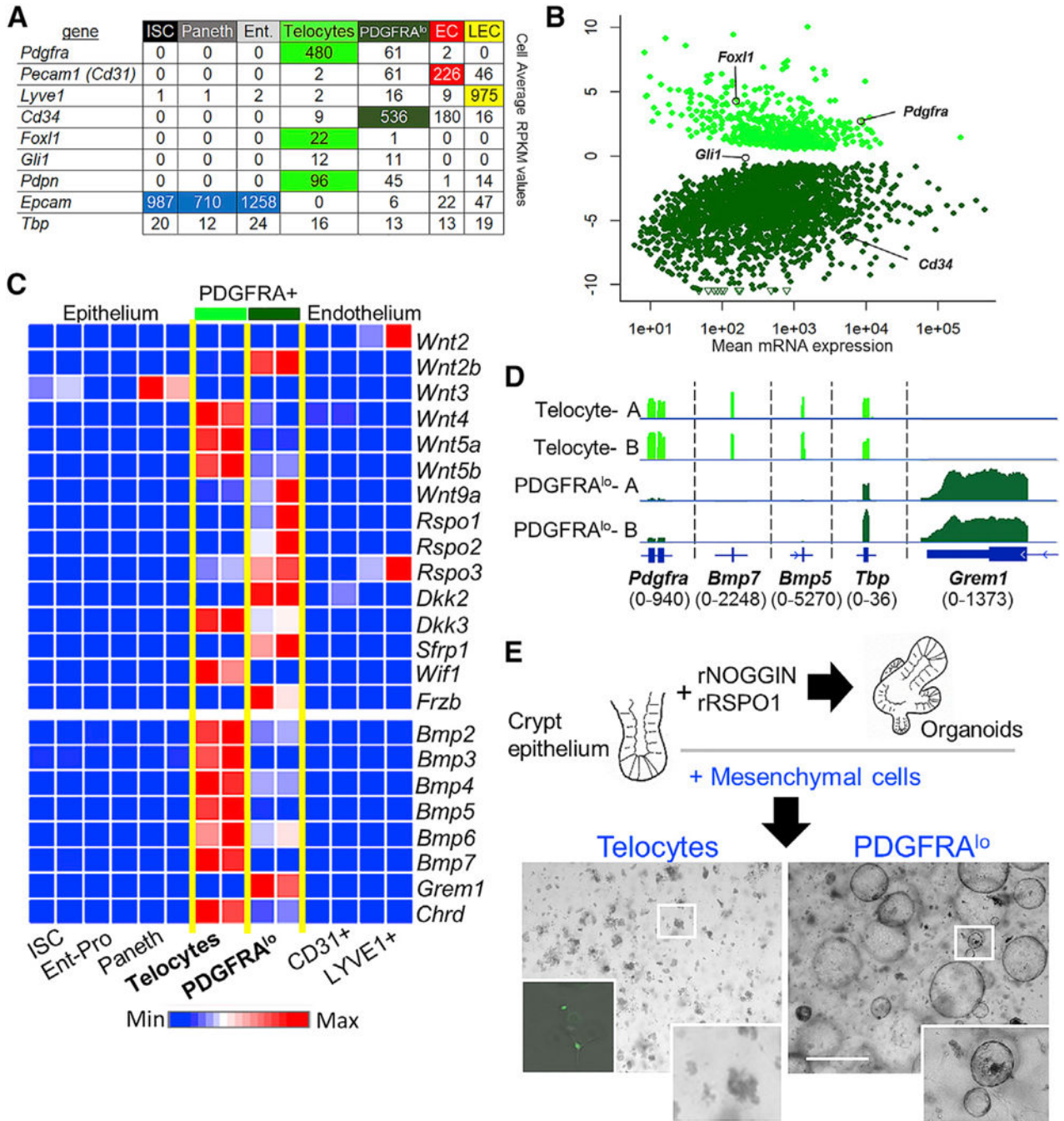


Figure 2. Distinct Niche Signals and Epithelial Supportive Functions of Intestinal Telocytes and PDGFRA^{lo} Stromal Cells

(A) Average normalized reads per kilobase per million (RPKM) values of known marker genes from duplicate RNA-seq libraries of the indicated cell types. Telocytes express the highest *Pdgfra* levels and alone express *Foxl1*, while PDGFRA^{lo} cells express *Cd34* and are the only other *Pdgfra*-expressing cell type. *Pdpn* and *Gli1*, markers recently ascribed to stromal cell populations (Degirmenci et al., 2018; Stzepourginski et al., 2017), express at roughly equal levels in telocytes and PDGFRA^{lo} cells. *Tbp*, a representative house-keeping gene, confirms accurate library normalization.

(B) Differential expression of >2,400 transcripts ($q < 0.05$, \log_2 fold-difference >1.5) in telocytes and PDGFRA^{lo} cells; selected genes are shown.

(C) Relative expression of secreted niche factor mRNAs in purified epithelial and mesenchymal cell populations, selected from a full set of Wnt and BMP pathway agonists and antagonists (Table S1). The heatmap is prepared from normalized values for RPKM averaged from duplicate RNA-seq libraries of each cell type.

(D) Integrative genome viewer (IGV) tracks showing RNA-seq data for *Bmp5*, *Bmp7*, *Grem1*, and *Pdgfra* in duplicate cell isolates. *Tbp* controls for proper normalization of read counts and the numbers in parentheses refer to the range of signal values.

(E) Co-culture of isolated mouse small intestine crypts in Matrigel, showing that PDGFRA^{lo} cells ($n = 12$), but not telocytes ($n = 7$, left inset shows viable GFP⁺ telocytes), substitute for recombinant factors NOGGIN and RSPO1 to generate abundant spherical enteroid structures. Boxed areas are magnified in the bottom right insets. Scale bar, 1 mm.

See also Figure S2 and Table S1.

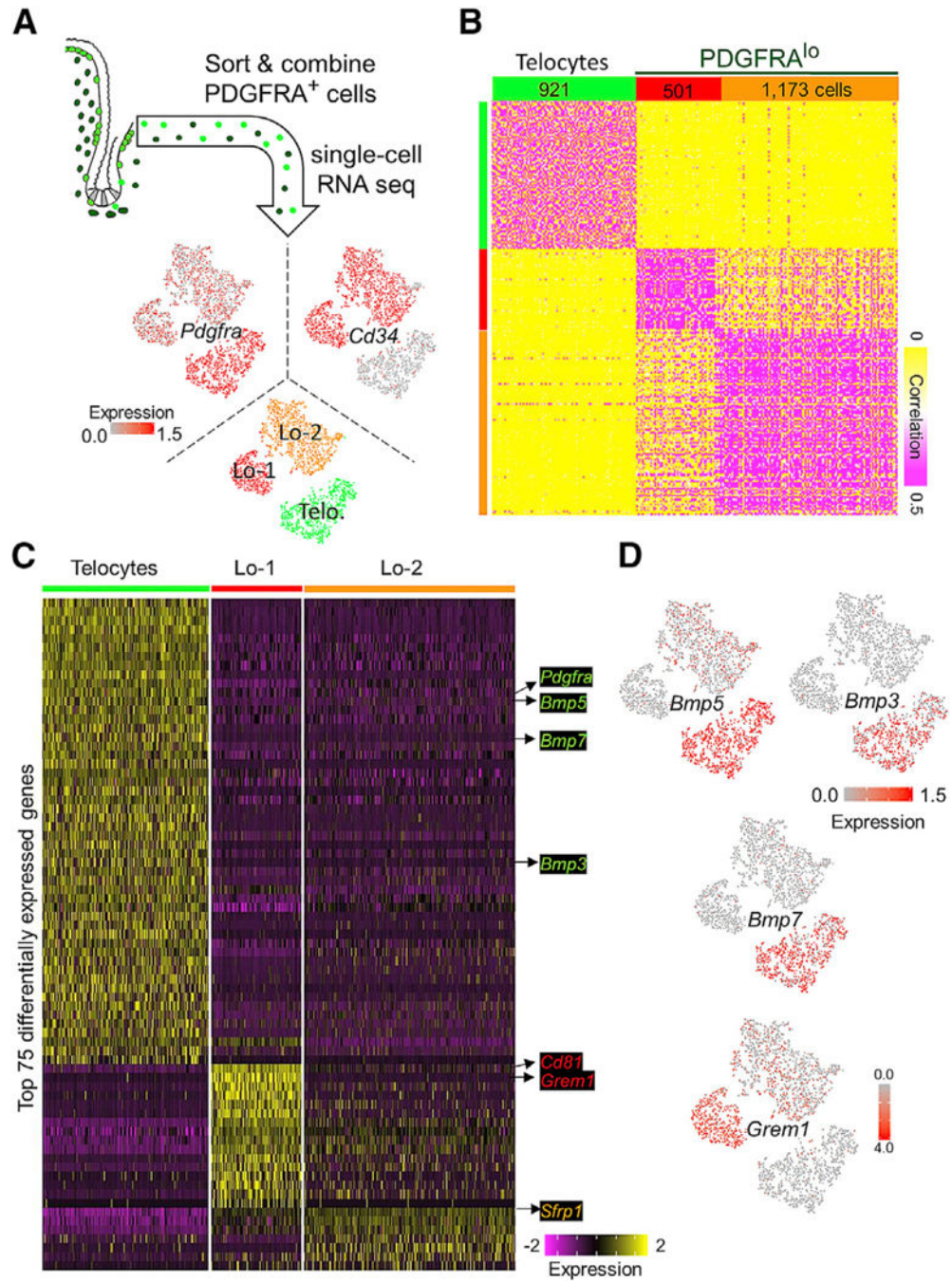


Figure 3. sc-RNA Sequencing Reveals Three Distinct PDGFRA⁺ Populations
 (A) GFP^{hi} and GFP^{lo} cells were sorted from *Pdgfra*^{H2BeGFP} mouse intestinal mesenchyme and combined for single-cell (sc) RNA-seq. t-Distributed stochastic network embedding (t-SNE) of data from 921 GFP^{hi} and 1,674 GFP^{lo} (PDGFRA^{lo}) cells reveals three populations. *Cd34*⁻ *Pdgfra*^{hi} telocytes are distinct from two novel *Cd34*⁺ PDGFRA^{lo} subpopulations.
 (B) Unsupervised clustering verified the similarities within, and differences between, the three cell groups.

(C) Genes differentially expressed among the three PDGFRA⁺ mesenchymal cell types ($p < 0.01$, average \log_2 fold change >1). BMP ligand transcripts are highly enriched in telocytes, *Cd81*, and *Grem1* are two of the three best distinguishers of Lo-1 cells, and *Stfp1* best distinguishes both PDGFRA^{lo} populations from telocytes.

(D) Projection of *Bmp5*, *Bmp3*, *Bmp7*, and *Grem1* single-cell transcript density onto the t-SNE map.

See also Figure S3 and Table S2.

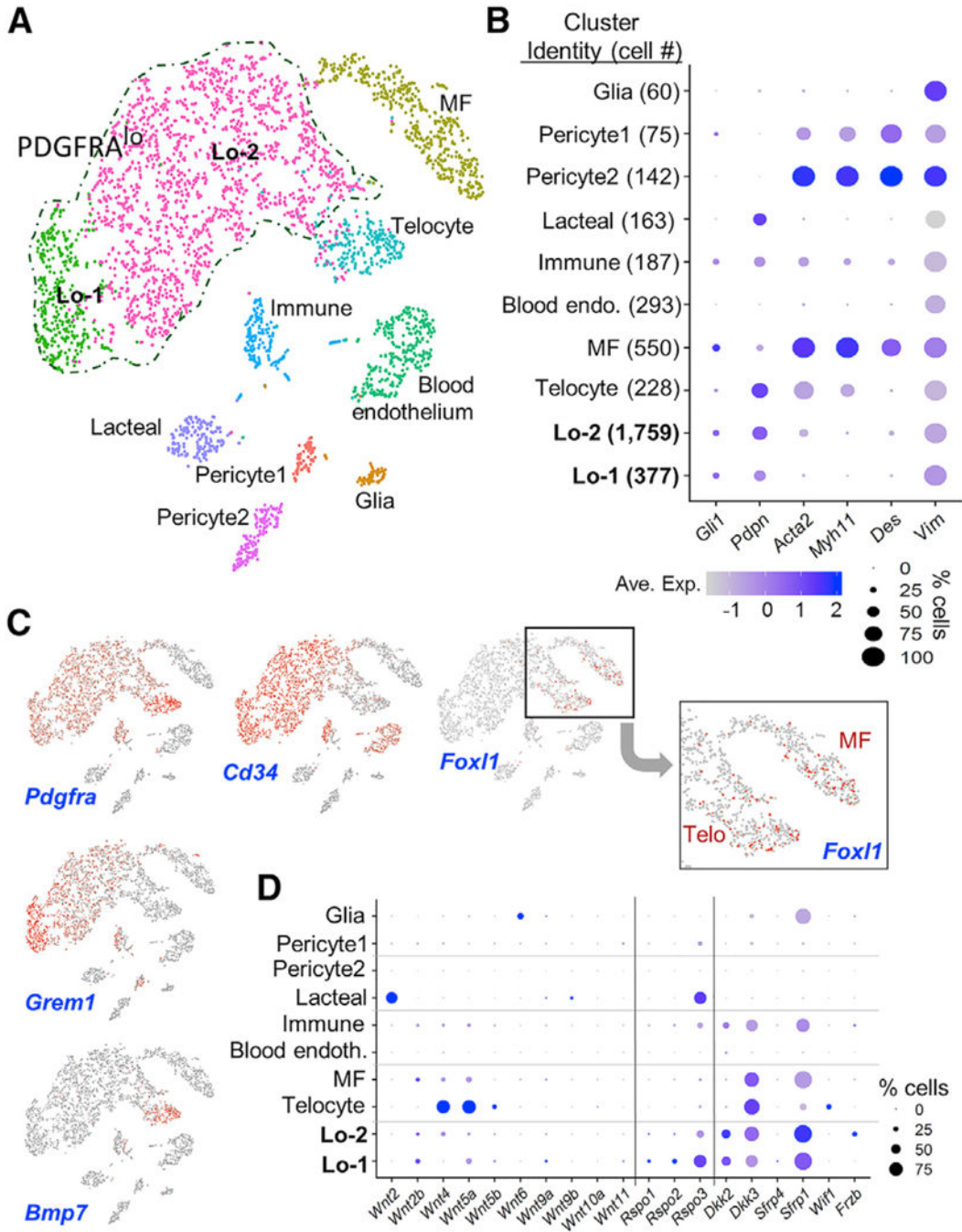


Figure 4. *Pdgfra*^{lo} Cells Are the Dominant Resident Population in the Small Bowel Mesenchyme
 (A) Clustering of 10 discrete cell populations by t-SNE of RNA profiles from 3,763 single mesenchymal cells, excluding *Ptprc*⁺ leukocytes.
 (B) Relative expression of known stromal cell markers in cell clusters identified by scRNA-seq. Circle sizes represent the within-cluster probability of gene detection and fill colors represent normalized mean expression levels.

Author Manuscript

Author Manuscript

Author Manuscript

Author Manuscript

(C) Projection of *Pdgfra*, *Cd34*, *Foxl1*, *Grem1*, and *Bmp7* single-cell transcript density onto the t-SNE map. *Foxl1*⁺ cell clusters are magnified, showing expression in both telocytes and MFs.

(D) Relative expression of Wnt, Rspo, and Wnt inhibitor transcripts in the single-cell clusters.

See also Figure S4.

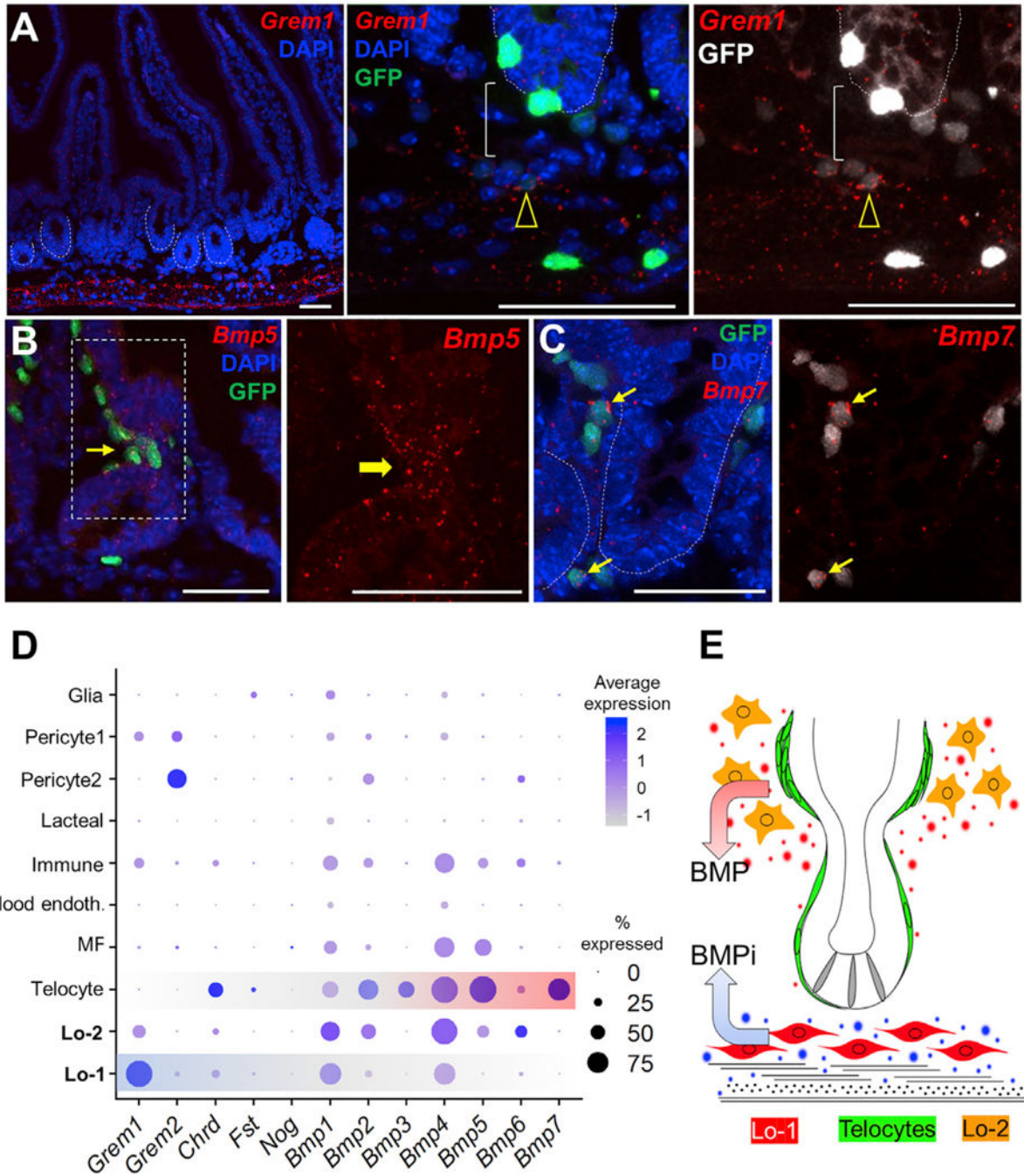


Figure 5. Spatial Polarity of *Grem1* and *Bmp* Expression

(A) RNA *in situ* hybridization localizes *Grem1* transcripts largely in two parallel stripes. Beneath the crypt epithelium (dotted outlines), confocal microscopy further localizes *Grem1* mRNA in PDGFRA^{lo} cells (arrowhead), revealing a gap (bracket) between these sub-cryptal cells and the epithelium. To highlight this gap, GFP signal is rendered in gray to the right. PDGFRA^{hi} pericryptal (telocytes) and muscularis (Purkinje-like) cells lack *Grem1*. Images represent dozens of microscopic fields examined in three independent experiments.

(B and C) *In situ* hybridization localizes *Bmp5* (B) and *Bmp7* (C) mRNAs in telocytes (arrows), which embrace the epithelium and concentrate at the crypt-villus boundary. Images represent dozens of microscopic fields examined in three independent experiments, and boxed regions are magnified in panels to the right. In light of the absence of *Bmp5* mRNA in crypt epithelial cells (Table S1), the faint epithelial signal is likely background noise. All scale bars, 50 μ m.

(D) Relative expression of BMP inhibitors and ligands in single-cell clusters identified in unfractionated mesenchyme.

(E) Model of the mesenchymal BMP gradient, showing telocytes (green) as the major and Lo-2 cells (orange) as possibly minor sources of BMP agonists concentrated at the villus base, with sub-cryptal Lo-1 cells (red) providing BMPi near the crypt base to oppose that signal (ISCs in gray).

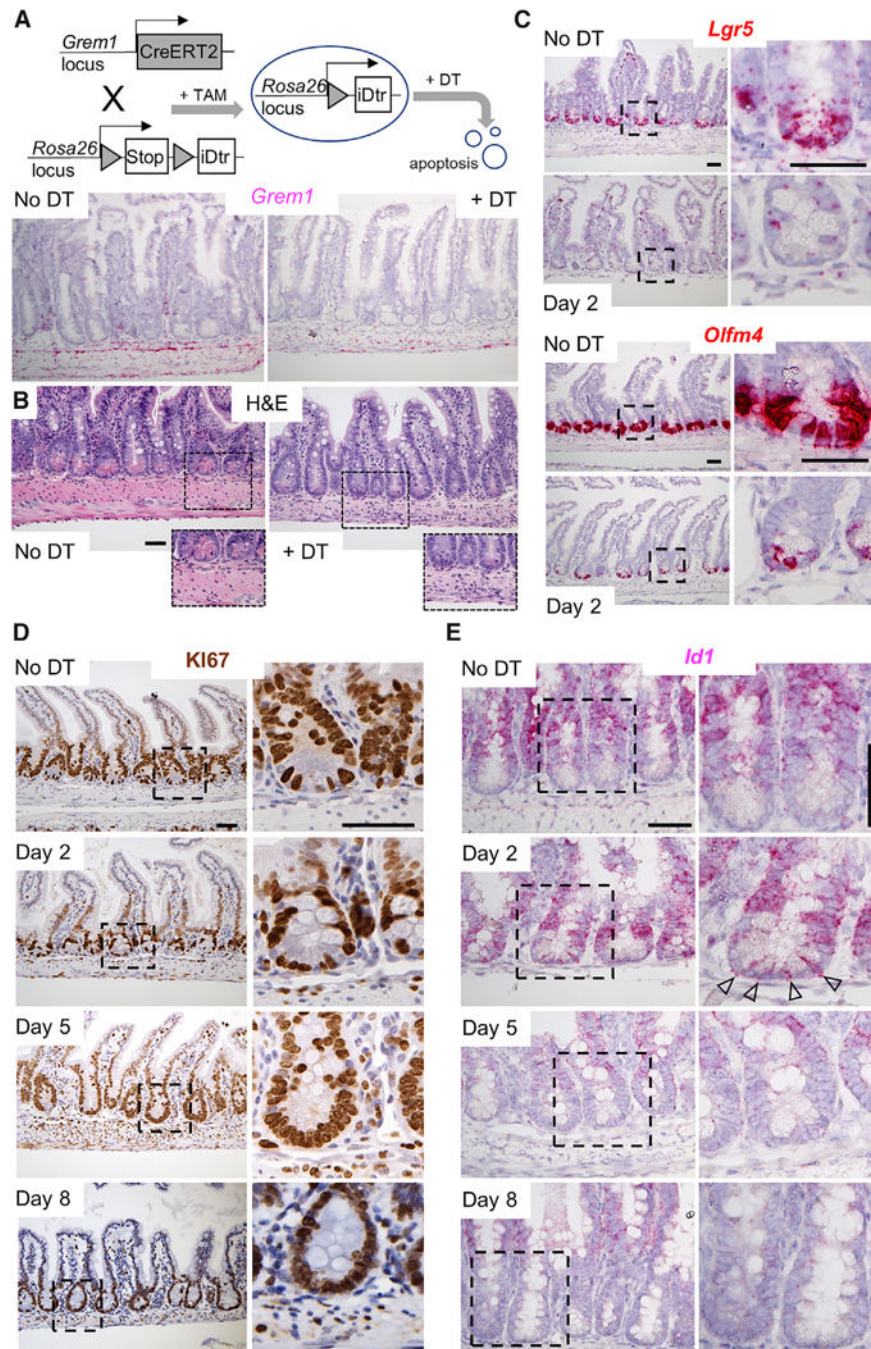


Figure 6. *Grem1*⁺ Mesenchymal Cells Sustain ISC *In Vivo*

(A) Targeting strategy for depletion of *Grem1*⁺ cells. Ablation of *Grem1*⁺ cells is verified by absence of *Grem1* mRNA (*in situ* hybridization) two days after the second of 2 DT injections.

(B) Histology (H&E) shows reduced external muscle, inflammatory infiltrates, and disrupted epithelial morphology within 5 days of *Grem1*⁺ cell ablation. Boxed regions are magnified in the insets.

(C) Expression of ISC markers *Lgr5* and *Olfm4* is markedly attenuated within two days of *Grem1*⁺ cell ablation.

(D) Replicating (KI67⁺) TA cells remain in intestines depleted of *Grem1*⁺ cells and occupy the crypt bottoms, which are depleted of *Lgr5*⁺ ISC.

(E) BMP target gene *Id1* is increased two days after *Grem1*⁺ cell ablation, selectively in crypt base columnar cells, and subsequently lost, coincident with ISC attrition.

All images depict data from three or four independent mice. Boxed areas in each image are magnified to the immediate right. All scale bars, 50 μ m.

See also Figures S5 and S6.

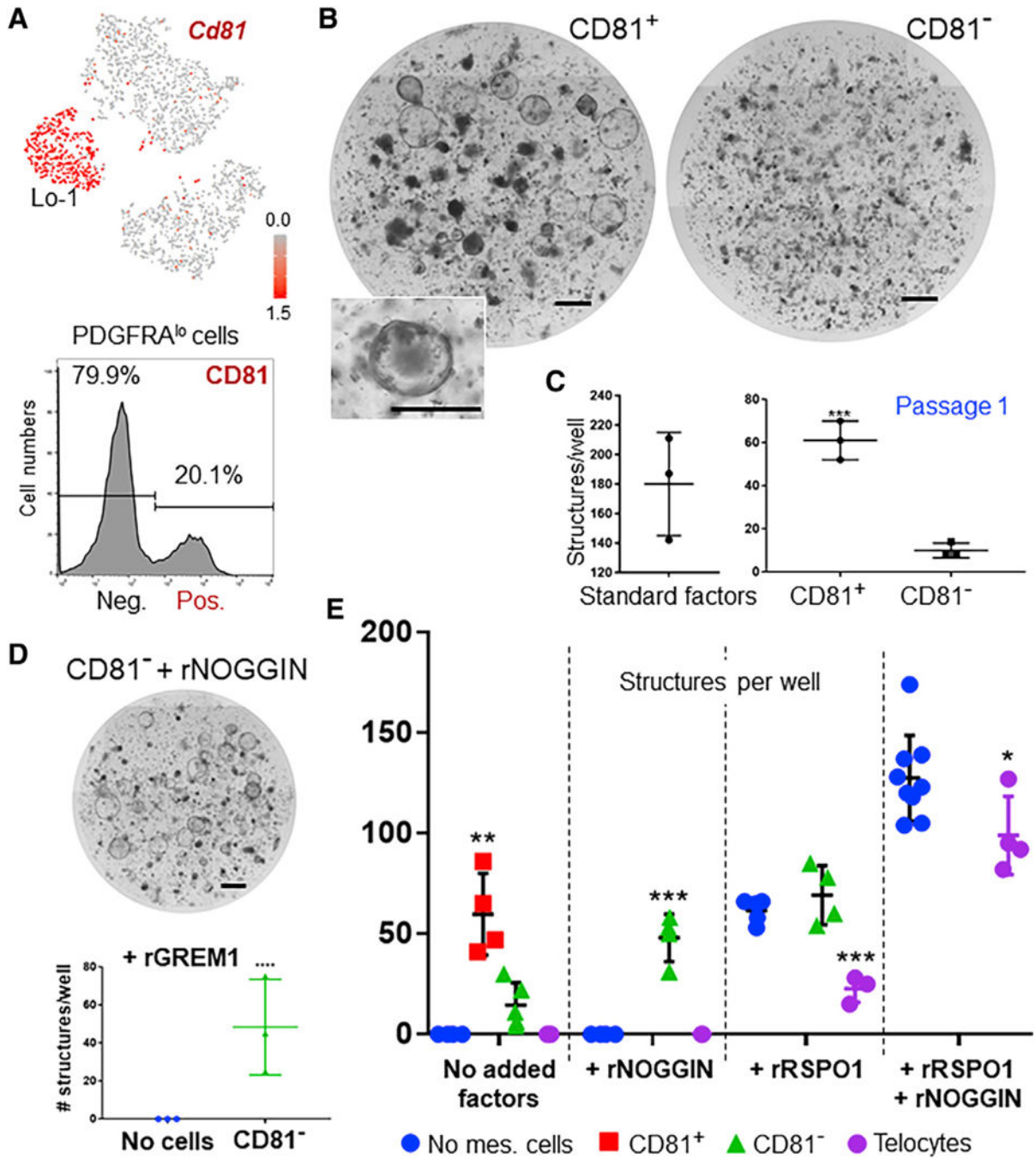


Figure 7. *Grem1*⁺PDGFRA^{lo} Cells Selectively Express CD81 and Support Enteroid Growth
 (A) Top: *Cd81* transcript levels projected onto the t-SNE map of scRNA-seq data (Figure 3), showing highly enriched expression in Lo-1 cells. Bottom: PDGFRA^{lo} cell separation into CD81⁺ and CD81⁻ subpopulations by flow cytometry with CD81 Ab.
 (B) Co-culture of isolated crypt epithelium with CD81⁺ and CD81⁻ PDGFRA^{lo} cells in the absence of recombinant trophic factors, showing enteroid growth stimulated by the CD81⁺ but not by the CD81⁻ fraction. Inset shows one magnified enteroid.

- (C) Successful propagation of structures produced in CD81⁺ co-cultures. Standard conditions: rRSPO1, rNOGGIN, and rEGF. n = 3 experiments each.
- (D) Addition of rNOGGIN or rGREM1 to CD81⁻ crypt co-cultures overcomes their inability to support enteroid growth.
- (E) Quantitation of spheroid structures from multiple (n, 3 to 5) experiments of crypt epithelium co-culture with the indicated mesenchymal cells and recombinant (r) factors. Bars represent mean \pm SEM values. Significance of differences was determined by two-tailed t test, one-way ANOVA.
- **p < 0.01; ***p < 0.001; n.s., not significant. All scale bars, 1 mm.
See also Figure S7.

KEY RESOURCES TABLE

REAGENT or RESOURCE	SOURCE	IDENTIFIER
Antibodies		
LYVE1	AngioBio	11-034; RRID: AB_2813732
CD31	BD	557355; RRID: AB_396660
NG2	Millipore	5320; RRID: AB_11213678
Laminin	Sigma	L9393; RRID: AB_477163
PDGFRA (IHC)	R&D Systems	AF1062; RRID: AB_2236897
PDGFRA (FACS)	Invitrogen	13-1401-80/12-1401-81; RRIDs: AB_466606 and AB_657615
Alpha-smooth muscle actin	Abcam	5694; RRID: AB_2223021
TUJ1	Abcam	18207; RRID: AB_444319
KI67	Gentex	16667; RRID: AB_422351
APC-conj. CD31	BD	551262; RRID: AB_398497
CD81	Invitrogen	13-0811-81; RRID: AB_466514
GFP	Abcam	6556/6662; RRIDs: AB_305564 and AB_305635
Podoplanin	Biologend	127410/127412; RRIDs: AB_10613649 and AB_10613648
Lysozyme	Dako	A0099; RRID: AB_2341230
Chemicals, Peptides, and Recombinant Proteins		
TrypLE Express	ThermoFisher	12604-021
Trizol reagent	ThermoFisher	15596026
Collagenase II	Worthington	LS004176
NOGGIN	Peptotech	120-10C
RSPONDIN1	R&D Systems	3710-001-01
EGF	ThermoFisher	PHG0311
GREMLIN1	ThermoFisher	956GR050
Matrigel	Corning	356231
Diphtheria Toxin	Enzo Life Sciences	BML-G135-0001
4-OH Tamoxifen	Sigma	T5648
DMEM/F12 Media	GIBCO	12634-010
Fetal Bovine Serum	Corning	35-010-CV
Penicillin/Streptomycin	Life Technologies	15140163
Glutamax	GIBCO	35050-661
N-2 Supplement (100X)	Life Technologies	17502001
B-27 Supplement (50X)	Life Technologies	17504001
NICOTINAMIDE	Sigma	72340
N-Acetylcysteine	Sigma	A9165
Normal Goat Serum	Cell Signaling	5425S
DAPI	BD PharMingen	5649097
DMEM	Corning	17-205-CV
HBSS (10X)	GIBCO	14065-056

REAGENT or RESOURCE	SOURCE	IDENTIFIER
PBS (10X)	Corning	46-013-CM
AlexaFluor Goat 546 anti-rat IgG	Invitrogen	A11081
AlexaFluor Goat 633 anti-rabbit IgG	Invitrogen	A21071
AlexaFluor 594 donkey anti-goat IgG	Invitrogen	A11058
Biotin	Invitrogen	17-4317-82
Bovine Serum Albumin	Sigma	A9647
Paraformaldehyde	EMS	15714-S
Picric Acid	Fluka	80456
FocusClear	CEIExplorer	FC-101
Triton X-100	Sigma	T8787
Sodium azide	Sigma	S2002
HEPES	Sigma	H3375
VectaShield mounting medium	Vector Laboratories	H-1000
Critical Commercial Assays		
RNAscope Multiplex Fluorescent Reagent Kit v2	ACD	323100
RNeasy microkit	QIAGEN	74004
SMART-Seq v4 Ultra Low Input RNA kit	Clontech	634890
Single Cell 3' V2 assay	10X Genomics	PN-120237
Deposited Data		
Raw and analyzed data	This paper; Tables S1 and S2	GEO: GSE130681
Mouse reference genome Mm10, GRCm38	Genome Reference Consortium	https://www.ncbi.nlm.nih.gov/grc/mouse
Epithelial RNA datasets	Jadhav et al., 2017	GEO: GSE83394; GSE71713
Experimental Models: Organisms/Strains		
Mouse: PdgfraH2BeGFP	The Jackson Laboratory	007669
Mouse: ROSA26iDTR	The Jackson Laboratory	007900
Mouse: Grem1CreER(T2)	This study	None
Mouse: ROSA26 ^{YFP}	The Jackson Laboratory	006148
Oligonucleotides		
Grem1 probes	ACD	314741
Bmp5 probes	ACD	401241
Bmp7 probes	ACD	407901
Lgr5 probes	ACD	312171
Olfm4 probes	ACD	311831
Id1	ACD	312221
Axin2	ACD	400331
Oligonucleotides	This paper	Figure S7C
Software and Algorithms		
VIPER	Cornwell et al., 2018	https://bitbucket.org/cfce/viper/
STAR	Dobin et al., 2013	https://github.com/alexdobin/STAR/releases

REAGENT or RESOURCE	SOURCE	IDENTIFIER
Integrated Genomics Viewer	Robinson et al., 2011	http://software.broadinstitute.org/software/igv/
DeSeq2	Love et al., 2014	https://bioconductor.org/packages/release/bioc/html/DESeq2.html
RSeQC	Wang et al., 2012	http://rseqc.sourceforge.net/
R	R Development Core Team, 2013	https://cran.r-project.org/bin/windows/
Corrplot	Wei et al., 2017	https://github.com/taiyun/corrplot
Morpheus	Broad Institute	https://software.broadinstitute.org/morpheus/
DeepTools	Ramírez et al., 2016	https://github.com/deeptools/deepTools
Seurat package v2.3.3	Butler et al., 2018	https://github.com/satijalab/seurat
Cell Ranger v2.1.1	10X Genomics	https://support.10xgenomics.com/single-cell-gene-expression/software/pipelines/latest/installation
ImageJ Fiji	Schindelin et al., 2012	https://imagej.net/Fiji/
MATLAB	The Mathworks Inc.	N/A
t-SNE algorithm	van der Maaten, 2014	https://lvdmaaten.github.io/tsne/
MAST algorithm	Finak et al., 2015	https://github.com/RGLab/MAST
ACD HybEZ II Hybridization System	ACD	321710
10X Genomics Controller	10X Genomics	N/A
Slide Spacers	Grace Bio-Labs	654002